Cell

Brainstem neuropeptidergic neurons link a neurohumoral axis to satiation

Graphical abstract

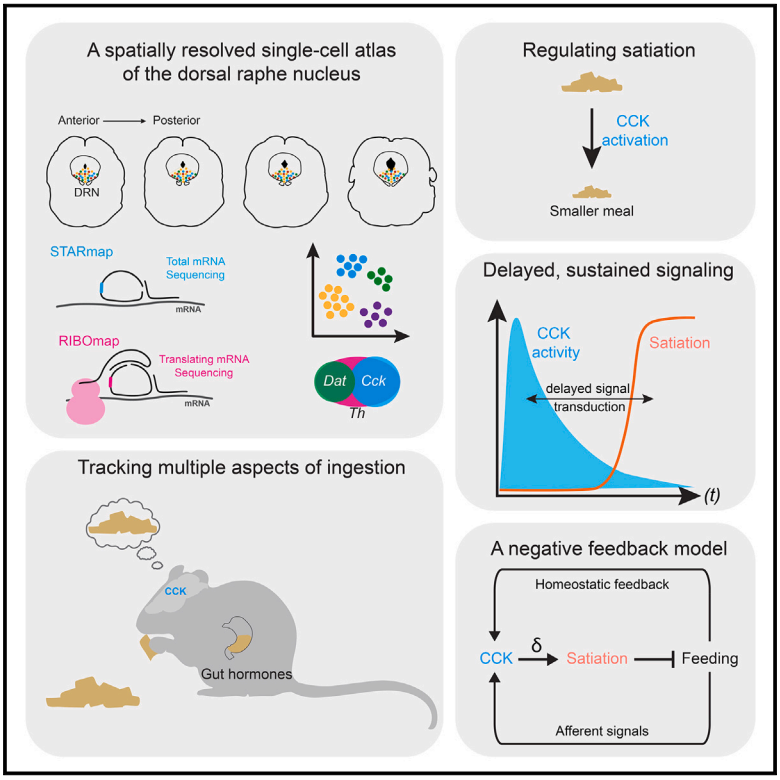

Highlights

- *In situ* molecular phenotyping of DRN at transcriptional and translational levels
- An obligate peptidergic population in the DRN is delineated by CCK expression
- CCK neurons track each bite of food to promote satiation via delayed signaling
- CCK neurons regulate satiation through multiple negative feedback loops

Authors

Srikanta Chowdhury, Nachiket G. Kamatkar, Wendy Xueyi Wang, ..., Hao Huang, Xiao Wang, Alexander R. Nectow

Correspondence

arn2136@columbia.edu

In brief

Use of spatially resolved molecular profiling identifies CCK neurons in the brainstem's dorsal raphe nucleus. These neurons track ingestion to promote satiation through a sustained signaling mechanism.

Chowdhury et al., 2025, Cell *188*, 1563–1579
March 20, 2025
https://doi.org/10.1016/j.cell.2025.01.018

CellPress

Cell

CellPress

Article

Brainstem neuropeptidergic neurons link a neurohumoral axis to satiation

Srikanta Chowdhury,[1,7] Nachiket G. Kamatkar,[1,7] Wendy Xueyi Wang,[2,3,4,7] Christa A. Akerele,[1] Jiahao Huang,[2,3] Junlin Wu,[1] Amajindi Nwankpa,[1] Charlotte M. Kane,[1] Varun M. Bhave,[1] Hao Huang,[5] Xiao Wang,[2,3] and Alexander R. Nectow[1,6,8,*]

[1]Department of Medicine, Columbia University, New York, NY 10032, USA
[2]Broad Institute of MIT and Harvard, Cambridge, MA 02142, USA
[3]Department of Chemistry, Massachusetts Institute of Technology, Cambridge, MA 02139, USA
[4]John A. Paulson School of Engineering and Applied Sciences, Harvard University, Boston, MA 02134, USA
[5]Princeton Neuroscience Institute, Princeton University, Princeton, NJ 08540, USA
[6]Division of Cardiology, Columbia University, New York, NY 10032, USA
[7]These authors contributed equally
[8]Lead contact
*Correspondence: arn2136@columbia.edu
https://doi.org/10.1016/j.cell.2025.01.018

SUMMARY

Hunger is evolutionarily hardwired to ensure that an animal has sufficient energy to survive and reproduce. Just as important as knowing when to start eating is knowing when to stop eating. Here, using spatially resolved single-cell phenotyping, we characterize a population of neuropeptidergic neurons in the brainstem's dorsal raphe nucleus (DRN) and describe how they regulate satiation. These neurons track food from sensory presentation through ingestion, integrate these signals with slower-acting humoral cues, and express cholecystokinin (CCK). These CCK neurons bidirectionally regulate meal size, driving a sustained meal termination signal with a built-in delay. They are also well positioned to sense and respond to ingestion: they express a host of metabolic signaling factors and are integrated into an extended network known to regulate feeding. Together, this work demonstrates how DRN CCK neurons regulate satiation and identifies a likely conserved cellular mechanism that transforms diverse neurohumoral signals into a key behavioral output.

INTRODUCTION

Hunger and satiety are evolutionarily conserved functions that ensure survival. These two opponent states enable animals to maintain proper energy stores by tightly balancing food intake with ongoing energy requirements. To initiate—and ultimately terminate—feeding, the brain needs to register a physiologic need, current or anticipated, and then convert that need into action. This requires processing of both internal (interoception) and external cues (exteroception), integrating these signals, and then transmitting instructions to carry out the complex and non-stereotyped appetitive sequences necessary to obtain food. Only at this point can feeding commence. Throughout this time, the animal must calculate what it will derive from a meal and plan when to stop eating. This process, which lies at the interface of hunger and satiety, is satiation.

Satiation, a negative feedback process that ultimately leads to meal termination, arises from monitoring many metabolic and ingestive parameters, most notably ongoing signaling from the oropharynx and gut.[1,2] Satiation is also dissociable from hunger and satiety signaling and is thus controlled by a distinct set of neural circuits. While hunger and satiety circuits are thought to originate in the hypothalamus,[3–6] classical studies utilizing decerebrate rats localized the regulation of satiation to the brainstem.[7–10] These studies demonstrated that the brainstem, independent of the forebrain, is sufficient to detect gastric loads and their associated "satiety signals" and appropriately respond by reducing food intake.[8,11,12] This work left a broad swath of the brainstem as a set of potential sites and cell types regulating satiation, leaving a longstanding, unresolved question: how does the brainstem appropriately terminate an ongoing meal?

Building on the pioneering work in decerebrate animals, more recent studies have delineated specific hindbrain cell types that terminate meals. These populations are largely confined to the nucleus of the solitary tract (NTS) and parabrachial nucleus (PBN)[9,13–15] and together detect the interoceptive signals of ingestion: they receive both vagal and spinal mechano- and chemosensory signals and consequently suppress appetite.[9] Many of these cell types also appear to play intertwined yet distinct roles from satiation, relaying various ingestive signals from the gastrointestinal (GI) tract, and in some cases serving as a more general alarm signal.[16,17] More recent work has also

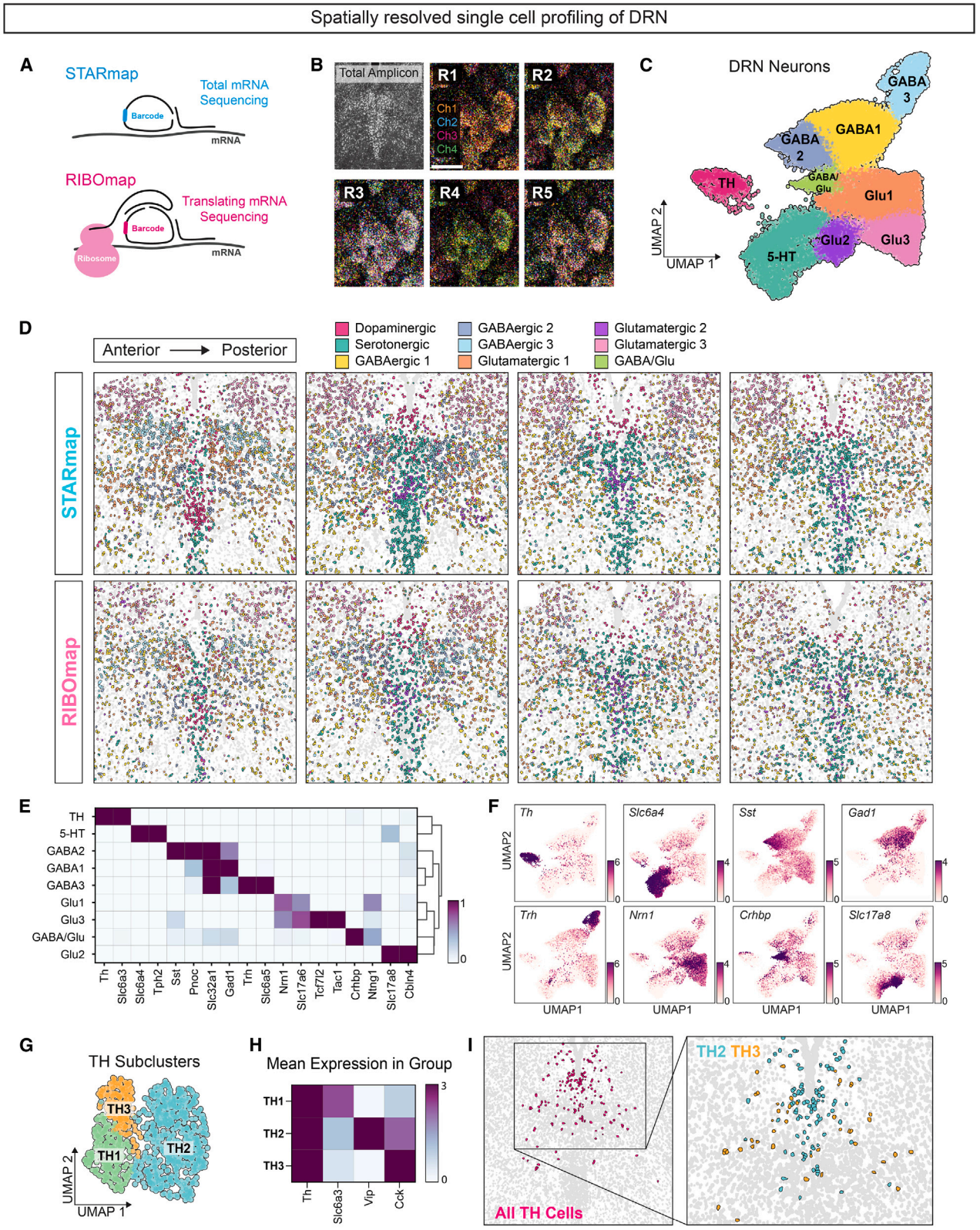

(legend on next page)

demonstrated a key role for the hindbrain in detecting orosensory and visceral ingestive signals to mediate the non-aversive suppression of appetite.[15,18,19] Critically, through poorly understood mechanisms, these sensory lines of information are integrated with other physiologic, cognitive, and behavioral variables at unknown downstream loci to drive meal termination.[20] So while known hindbrain circuits integrate distinct lines of viscerosensory/interoceptive information to regulate feeding, they do not appear to be the sole mediators of satiation.[15] These studies, in aggregate, suggest the existence of higher-order processing within the brainstem to terminate feeding.

Evidence for higher-order processing of feeding-related functions within the brainstem arises, in part, from detailed and cell-type-specific neuroanatomical studies. Projection mapping from ascending structures such as the NTS and PBN has identified, among other targets, the midbrain's dorsal raphe nucleus (DRN) and nearby ventrolateral periaqueductal gray (vlPAG) as key output structures.[21–25] Supporting an integrative role for the dorsal midbrain in regulating feeding are neuroanatomical and functional studies that identify these neurons as convergence points for descending modulatory projections from forebrain feeding centers.[26–29] Indeed, early lesion and pharmacological manipulation studies,[30–33] as well as more recent genetic manipulations,[34–37] have demonstrated that distinct cell types in the DRN/vlPAG can bidirectionally regulate feeding. While recent work has questioned a specific role for hypothalamic modulation of appetite via the dorsal midbrain,[28,38] the above work suggests that this area may play an outsized, yet underappreciated role in regulating distinct aspects of feeding.[28]

Here, we describe how physiologic and behavioral variables are integrated with oro- and viscerosensory information in the brainstem to regulate meal size. Using single-cell, spatially resolved molecular profiling, we find that DRN neurons expressing cholecystokinin (CCK) comprise a unique neuropeptidergic subpopulation, with a molecular composition enabling them to sense and respond to diverse metabolic cues. These CCK neurons integrate longer-term neurohormonal signals with acute food-related sensory variables to terminate meals. These neurons are activated by food intake, as well as cues signaling or predictive of consumption. We also find that these neurons sense gut-borne signals via mechano- and chemosensory relays, as well as their elicited neurohormonal cues. Consequently, through a phasic, yet sustained negative feedback mechanism, CCK neurons suppress food intake through meal termination. Contextualizing these findings, we demonstrate that CCK neurons are integrated into the extended network known to regulate feeding, receiving convergent inputs from diverse sensory structures and funneling them into selective outputs in the forebrain and hindbrain. Together, this work presents a framework to understand the central regulation of satiation and introduces CCK neurons as a key entry point for studying this essential process.

RESULTS

A spatially resolved molecular map of the DRN at single-cell resolution

The DRN is molecularly heterogeneous, hindering prior attempts to understand its role in diverse behavioral and physiological processes. To better characterize this region, we turned to spatially resolved transcriptomic and translatomic profiling approaches with single-cell resolution[39,40] (Figures 1A and 1B). This class of *in situ* profiling approaches offers several key advantages, including spatial resolution, freedom from gene expression changes induced by cellular isolation, and consequently, greatly reduced bias in cell selection. We curated a list of 256 genes (Table S1), representing highly variable genes from previously published RNA sequencing (RNA-seq) studies.[36,41,42] Using this gene panel, we performed transcriptional and translational profiling, respectively, using STARmap and RIBOmap,[39,40] integrated these datasets using Harmony,[43] and annotated clusters, as previously described.[40,44] We additionally integrated these data with a previously published single-cell atlas of the DRN,[45] which was particularly useful for non-neuronal cell-type assignment. With this approach, we characterized over 85,000 high-quality cells and successfully decoded their cell-type identities (Figures 1C and S1A–S1E). All cell types were easily differentiable with single (or, in rare cases, two) marker genes (Figures S1F and S1G).

We next subsetted all neurons, which comprised ~40% of all DRN cells sequenced in our study (Figure 1C). As expected, we enriched for all principal cell types within the DRN (Figures 1D–1F). Most of these cell types had distinct spatial patterning along the anterior-posterior axis, which accorded well with their principal marker gene expression, as observed in the Allen Brain Atlas[46] (Figures 1D and S2A). Most of the molecular heterogeneity stemmed from the GABAergic and glutamatergic neurons (Figures 1E and S2A). We also noted a small population of putatively dual glutamatergic/GABAergic neurons, consistent with prior a report.[45] DRN serotonergic neurons have well-characterized subpopulations[41,42,45,47]; thus, we did not make further attempts to subcluster these neurons.

Figure 1. Single-cell spatially resolved transcriptomic and translatomic profiling of the DRN

(A) Schema for STARmap and RIBOmap *in situ* sequencing.
(B) Representative images for STARmap measurements across five sequencing rounds.
(C) Uniform manifold approximation and projection (UMAP) of DRN neurons.
(D) Clusters identified in (C) projected onto their respective spatial positions in DRN.
(E) Heatmap of expression for top differentially expressed transcripts for each neuronal cluster.
(F) UMAP displaying expression patterns for cluster-specific transcripts.
(G) UMAP for three TH+ neuronal subclusters.
(H) Differentially expressed transcripts among TH+ subclusters.
(I) TH+ subclusters identified in (G) are projected onto their spatial positions.
Scale bar, 20 μm. Color scales indicate *Z* scored expression values.
See also Figures S1 and S2 and Table S1.

We next focused on the molecular composition of the dopaminergic cluster, which has not been well characterized. This cluster comprised ~3% of DRN neurons and appeared to be heterogeneous, with three distinct cell subtypes (Figure 1G). All three subtypes expressed *Th* mRNA at high levels but variably expressed other marker genes typically representative of dopamine-releasing neurons (Figures 1H and S1H). All three subpopulations appeared to be devoid of fast neurotransmitter marker gene expression. Comprising around a quarter of TH+ cells, the TH1 subcluster exhibited a gene expression profile characteristic of dopaminergic neurons. These neurons expressed high levels of classical dopaminergic marker genes, including the dopamine transporter *Slc6a3*, vesicular monoamine transporter *Slc18a2*, dopamine neuron developmental marker *Nr4a2*, and key monoamine synthetic enzymes *Ddc* and *Gch1* (Figure S1H). By contrast, these markers were expressed at substantially lower (or undetectable) levels in the other subclusters, TH2 and TH3 (Figures 1H and S1H).

These latter two subclusters were molecularly differentiated by the presence (TH2) or absence (TH3) of *Vip* expression, and both were defined by high levels of *Cck* expression (Figure 1H). We confirmed these findings using hybridization chain reaction fluorescence *in situ* hybridization (HCR-FISH; Figures S2B–S2E). *Cck* expression thus marks a well-defined, but previously unexplored, subpopulation of TH+ DRN neurons that are predominantly non-dopaminergic and appear to be obligate peptidergic (Figure 1I). Given that CCK peptide, itself, and CCK-expressing neurons elsewhere in the brain are known to control feeding,[48–50] we sought to more comprehensively characterize this unique population by molecularly profiling CCK neurons at scale.

CCK delineates a small population of neuropeptidergic DRN neurons

We performed ensemble-level molecular profiling of CCK neurons using viral-based translating ribosome affinity purification (vTRAP).[51–53] The vTRAP technique confers specificity to actively translated mRNAs by tagging the large ribosomal subunit.[54,55] Using vTRAP in tandem with RNA-seq, we profiled CCK-expressing neurons (Figures 2A and 2B), significantly enriching for key control mRNAs *Rpl10a* and *Cck* while significantly depleting for non-neuronal marker genes (Table S2). This demonstrated that high-quality RNA was precipitated specifically from *Cck*-expressing neurons in DRN.

We next examined the neuropeptide composition of these neurons. Consistent with our single-cell studies, we significantly enriched for *Vip* and *Npw*, as well as many other neuropeptides, including *Cartpt* (Figure 2C; Table S2). We also significantly enriched for *Th* and *Ddc* but notably not *Slc6a3* or *Slc18a2* (Figure 2D; Table S2). We found no significant enrichment for any marker genes representing fast neurotransmitters (Figures 2C and 2D). However, this does not preclude the possibility that CCK neurons express low levels of these transcripts or non-canonically scavenge for and release glutamate and/or GABA, similar to other neurons expressing markers for dopamine synthesis.[56–58] However, we did not enrich for any markers of extracellular GABA transport, non-canonical GABA synthesis, or glycine synthesis/transport, and we significantly depleted for key serotonergic neuron marker genes (Figure 2D). These ensemble-level results are consistent with our STARmap/RIBOmap studies and point to an obligate peptidergic DRN cell type that partially overlaps with TH+ neurons.

We next performed Gene Ontology (GO) analysis[59] of the top 100 immunoprecipitation (IP)-enriched genes. This demonstrated significant pathway enrichment for neuropeptide signaling and pathways relevant to energy homeostasis (Figure 2E; Table S3). These neurons accordingly expressed a diverse array of signaling molecules, enzymes, and receptors key for metabolism, including those regulating the generation of energy and metabolites, nucleotide and peptide biosynthesis, and nutrient sensing (Table S4). While it is not possible to exclude the possibility of rapid neurotransmission without electrophysiologic studies, the above results are consistent with an obligate neuropeptidergic cell type with a molecular composition that is well positioned to regulate energy balance.

DRN neuropeptide neurons suppress appetite

Given our prior results finding a role for the DRN in regulating energy homeostasis,[34–36] we next investigated whether CCK neurons could influence appetite. We first performed Fos labeling and found significant Fos expression in CCK neurons in the refed state, but not in mice fed *ad libitum* or fasted overnight (Figures S3A and S3B). These histological studies, in tandem with our molecular profiling data, further suggested a potential role for CCK neurons in regulating energy balance.

To address this hypothesis, we optogenetically activated CCK neurons using ChR2[60] (Figure 2F). We found that stimulation of CCK neurons rapidly and reversibly suppressed food intake on the order of minutes (Figure 2G). This effect was scalable, with almost no food consumed during optogenetic activation at the highest frequency tested (Figures S3C–S3E). These data suggest that CCK neurons are dynamically regulated by metabolic and/or behavioral state and that they leverage this information to scalably suppress feeding. Critically, these neurons did not influence drinking (Figure 2H), and activating these neurons increased locomotor activity but was not anxiogenic and trended toward but had no significant effect on aversion (Figures S3F and S3G). Together, our results demonstrate that CCK neurons are activated by re-feeding and consequently suppress food intake in a rapid fashion.

Meal-time dynamics are encoded by phasic neural activity

We next explored what types of information CCK neurons use in real time to suppress feeding. We sought to answer this question by monitoring the natural activity patterns of these neurons during freely moving behavior. Given that these neurons were grossly activated by re-feeding, we hypothesized that they could be modulated in one of two ways: either on a bite-to-bite basis or from meal to meal (Figure 3A). On a bite-to-bite basis, these neurons could either signal in a tonic mode (and thus integrate each bite over the course of a meal) or a phasic mode (signaling bite-to-bite with no integrated neural activity). On a meal-to-meal basis, these neurons could fire in one of two phasic modes, encoding either the onset or offset of a meal. We set out to systematically test these hypotheses using *in vivo* calcium imaging with fiber photometry[61] (Figure 3B).

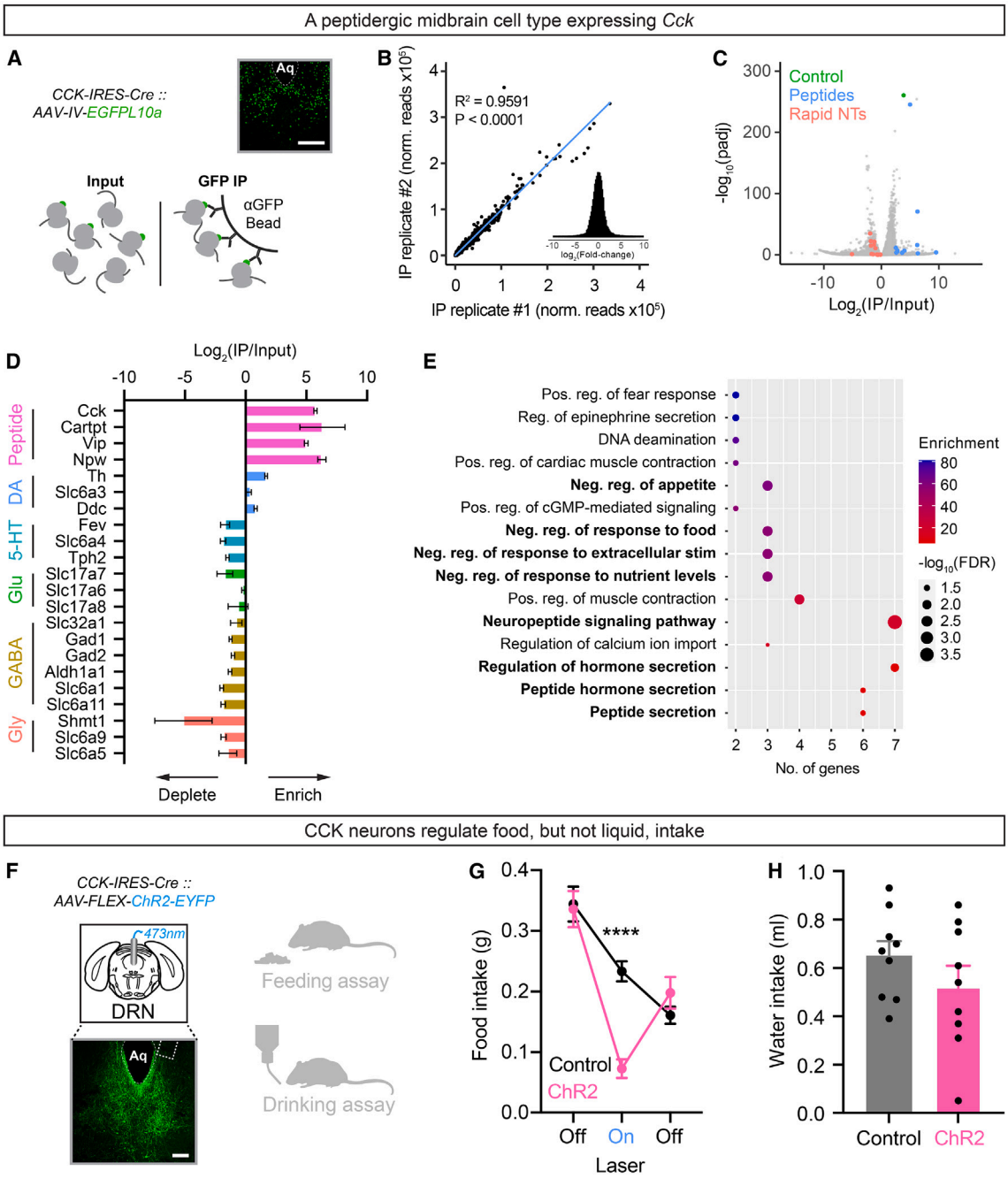

Figure 2. CCK delineates a likely obligate peptidergic appetite-suppressing population of DRN neurons

(A) Schema for vTRAP experiment with IHC inset (Aq, cerebral aqueduct).

(B) IPs are highly replicable (one outlier removed – expression > 57× SD than the second highest-expressed gene). Inset, histogram of $\log_2$ fold-enrichments (IP/input; $n = 2$ biological replicates).

(C) Volcano plot with $\log_2$ fold-enrichments. Control gene is *Rpl10a*.

(D) Enrichments for DRN-specific and glycinergic marker genes.

(E) GO analysis of the top 100 most enriched genes. Redundant categories were removed from the plot (see Table S3 for a full list).

(F) Schema for optogenetic activation of CCK neurons.

(G) Activation of CCK neurons acutely suppresses food intake ($n = 12–14$ mice per group).

(H) CCK neurons do not affect water intake ($n = 9$ mice per group).

Scale bar, 200 μm. ****$p < 0.0001$. Sequencing data are presented as mean ± lfcSE (standard error for log2 fold change). Behavioral data are presented as mean ± SEM. See also Figure S3 and Tables S2, S3, and S4.

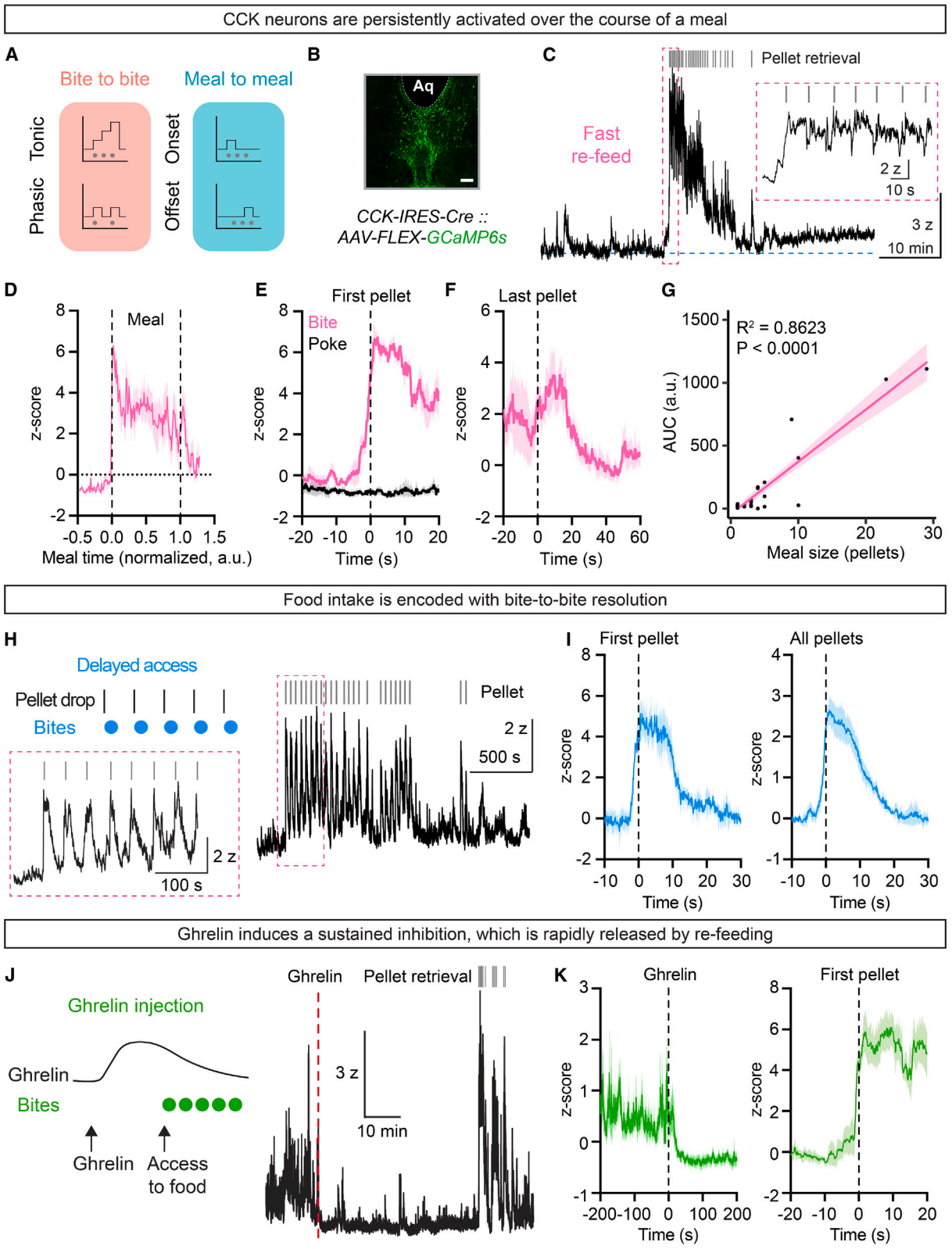

(legend on next page)

First, we took overnight-fasted mice and allowed them to re-feed using the FED3.0 automated feeding system,[62] enabling us to precisely time-lock neural events to bouts of consumption. We found that CCK neuron activity robustly responded to pellet retrieval, but not other motor activity, such as nose poking in the immediate vicinity of the trough (Figures 3C and 3E). In response to feeding, neural activity initially peaked after the first bite of food, corresponding to the onset of chewing (Figures 3E and S4A), and remained at an elevated baseline over the course of a meal (Figure 3D). After the last pellet was retrieved, there was a ~10 s delay (while the animal was completing consumption), after which activity slowly decayed toward baseline (Figure 3F). These effects occurred regardless of meal size, suggesting that these cells may tonically encode a meal. Consistent with this hypothesis, we also found that integrated CCK neuron activity during a meal scaled with meal size (Figure 3G). However, upon closer inspection of individual traces, we also noticed a clear phasic signal from pellet to pellet (Figures 3C and S4B). These findings suggest that, while CCK neurons may passively encode meal size through persistently elevated activity, they appear to be able to resolve out individual bites of food.

The neural dynamics we observed for CCK neurons during re-feeding are somewhat analogous to a leaky integrator, where the full signal from individual pellets may be masked by decaying neural activity from prior pellets retrieved. To test whether CCK neurons are capable of tracking bite-to-bite dynamics, we trained animals on a delayed-access feeding schedule. From the above studies, it appeared that CCK activity returned to baseline within ~30 s of pellet consumption. We thus repeated these studies but retrained the animals for access to food only after 30 s had elapsed since consumption of a prior pellet (Figure 3H). This would allow us to confirm whether persistently elevated activity during a meal was a key property of these neurons or a simple consequence of their leaky integrator-like properties. During this spaced-out feeding paradigm, single bites of food elicited robust activation of CCK neurons. Intriguingly, this signal returned to baseline within ~20 s after retrieval of a pellet, whether the animal consumed a single pellet in isolation or during the course of a protracted meal (Figures 3H and 3I). Together, these studies demonstrate that CCK neurons can resolve out individual bites of food, using phasic, bite-to-bite signaling. And due to their intrinsic cellular and/or network properties, the integrated activity of these neurons also appears to passively and reliably track meal size (Figure 3G).

We next asked whether these neurons could integrate other lines of information, such as slower-acting humoral signals. To answer this question, we took mice fed *ad libitum* and recorded from CCK neurons before and after injection of the orexigenic hormone ghrelin (Figure 3J). We found that ghrelin induced rapid and sustained silencing of CCK neurons, lasting up to tens of minutes (Figures 3J, 3K, and S4D). This finding, along with our results above, suggests that CCK neurons are capable of integrating diverse signals across broad timescales to regulate feeding. In further support of this notion, we also found that this sustained inhibition could be rapidly released by access to and consumption of chow (Figures 3J and 3K). This rapid behavioral release from ghrelin-induced inhibition, together with the lack of significant enrichment for ghrelin's receptor (growth hormone secretagogue receptor, *Ghsr*) in our vTRAP dataset (Table S2), suggests that these neurons are likely not directly modulated by ghrelin but are tonically inhibited by an upstream population that directly senses circulating ghrelin.

Feeding can be inhibited by stimuli unrelated to energy balance, such as those resulting in threat, aversion, or fear.[17] We next asked whether CCK neurons could be activated by these non-feeding-related, yet appetite-suppressing, cues. Consistent with a role for these neurons in specifically regulating adaptive feeding responses, exposure to tail pinch or fox odor (trimethylthiazoline [TMT]) was both unable to elicit changes in CCK neuronal activity (Figure S4C). Together, these studies demonstrate that CCK neurons can detect diverse non-aversive neurohormonal signals over broad timescales to adaptively regulate feeding.

DRN neuropeptide neurons regulate meal termination

Brobeck initially pointed out that in animals eating periodically, total food intake is the product of average meal size and meal frequency.[63] The phasic natural activity patterns of CCK neurons and their rapid suppression of food intake would appear to support a role for these neurons in the shorter-term control of a meal. To test this hypothesis, we optogenetically activated these neurons while performing a re-feeding task, again using the FED3.0 system[62] to track the microstructure of food consumption. As demonstrated previously, optogenetic activation of CCK neurons led to a significant suppression of food intake over the course of an hour (Figures 4A, left, and S5A). Further analysis of meal-time dynamics demonstrated a substantial shift in the distribution of pellet consumption (Figure 4A, right), which was

Figure 3. Phasic encoding of mealtime dynamics with bite-to-bite resolution

(A) Schema for possible encoding mechanisms used by CCK neurons (x axis is time, y axis is neural activity, and dots below each trace represent pellets consumed).

(B) Immunohistochemistry (IHC) showing labeling of CCK neurons with genetically-encoded calcium indicator GCaMP6s.

(C) Sample trace of CCK neuronal activity during fast-refeeding. Inset, magnified trace.

(D) CCK neuronal activity during the first meal, normalized (n = 4 mice).

(E and F) CCK neuronal activity time-locked to the first (E) or last (F) bite of the first meal (n = 4 mice).

(G) Integrated neural activity linearly scales with meal size.

(H) Schema for delayed-access feeding regimen (left) with sample trace of neuronal activity (right). Inset, magnified portion of one bout.

(I) CCK activity is time-locked to bites of food: (left) first bite and (right) all bites (n = 4 mice).

(J) Schema for ghrelin injection study (left) and sample trace of neuronal activity during a full recording session (right).

(K) Averaged activity traces for CCK neurons after ghrelin injection (left) and consumption of the first pellet after food access was granted (right) (n = 5–6 mice).

Scale bar, 200 μm. Data are presented as mean ± SEM (except for G, which is ± 95% CI).

See also Figure S4.

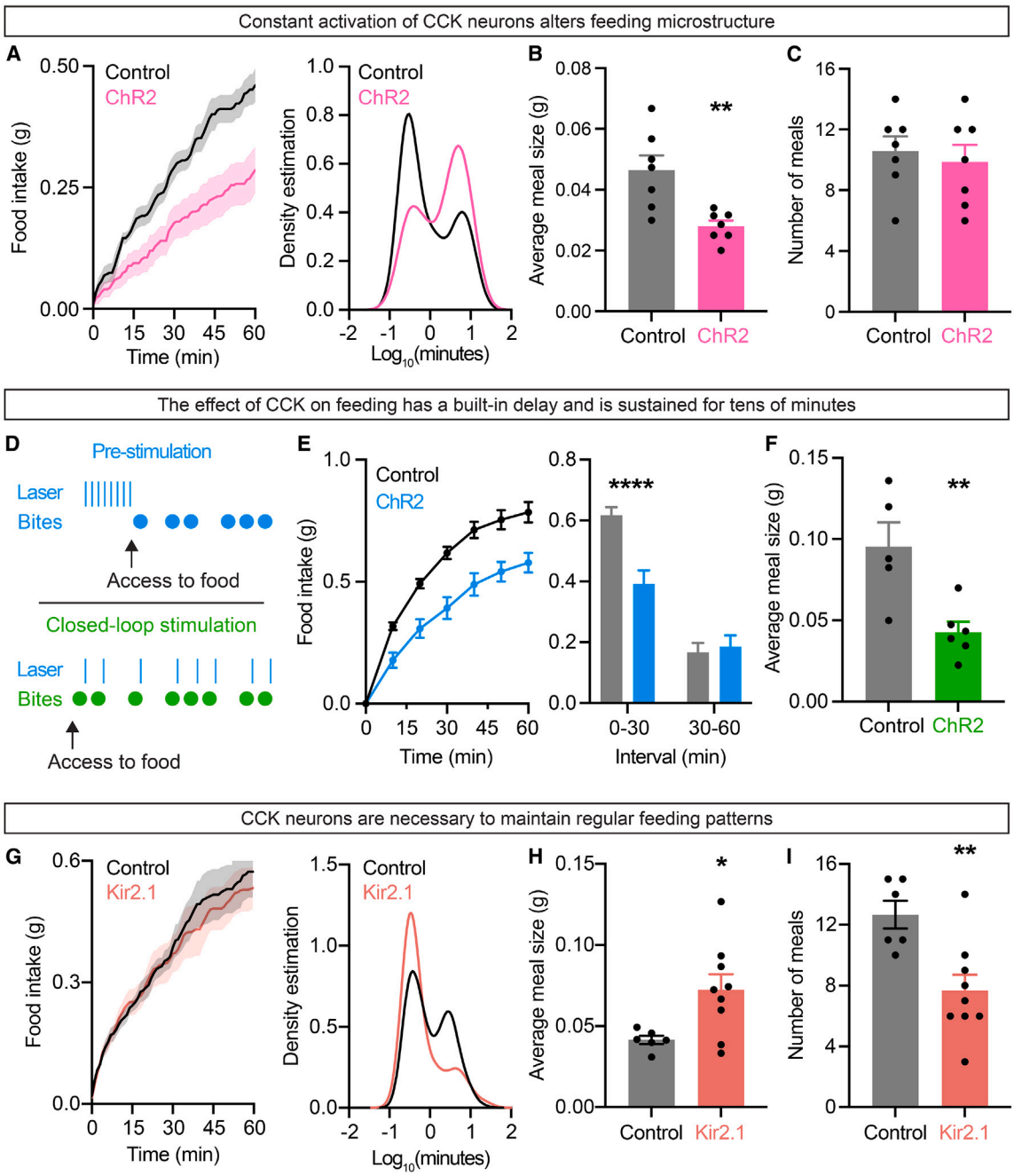

Figure 4. CCK neurons regulate meal termination via a short-lived yet hysteretic signal with a built-in delay

(A) Cumulative food intake is significantly altered (left) and affects feeding dynamics (inter-pellet intervals, right) (n = 7 mice per group).

(B and C) Average meal size is significantly suppressed in CCK::ChR2 mice (B), and the total number of meals is unaltered (C).

(D) Schema for experimental manipulations. (Top) Pre-stimulation: fasted animals receive 1 hr of pre-stimulation, followed by re-feeding. (Bottom) Closed-loop stimulation: mice receive brief optogenetic stimulation after each pellet retrieval.

(E) Pre-stimulation of CCK neurons reduces food intake over the course of an hour (left), and this effect is fully attributable to a reduction in feeding within the first 30 min of re-feeding (right; n = 9–10 mice per group).

(F) Closed-loop stimulation of CCK neurons reduces meal size with a built-in delay (n = 5–6 mice per group).

(G) Cumulative food intake is unaffected (left), whereas feeding dynamics (inter-pellet intervals, right) are altered in animals with chronic inhibition of CCK neurons using Kir2.1 (n = 6–9 mice per group).

(H and I) Average meal size is significantly increased in CCK::Kir2.1 mice (H), and meal frequency is decreased (I).

Scale bar, 200 μm. *$p < 0.05$, **$p < 0.01$, ****$p < 0.0001$. Data are presented as mean ± SEM. Inter-pellet intervals in (A) and (G) are shown as kernel density estimates. See also Figures S5 and S6.

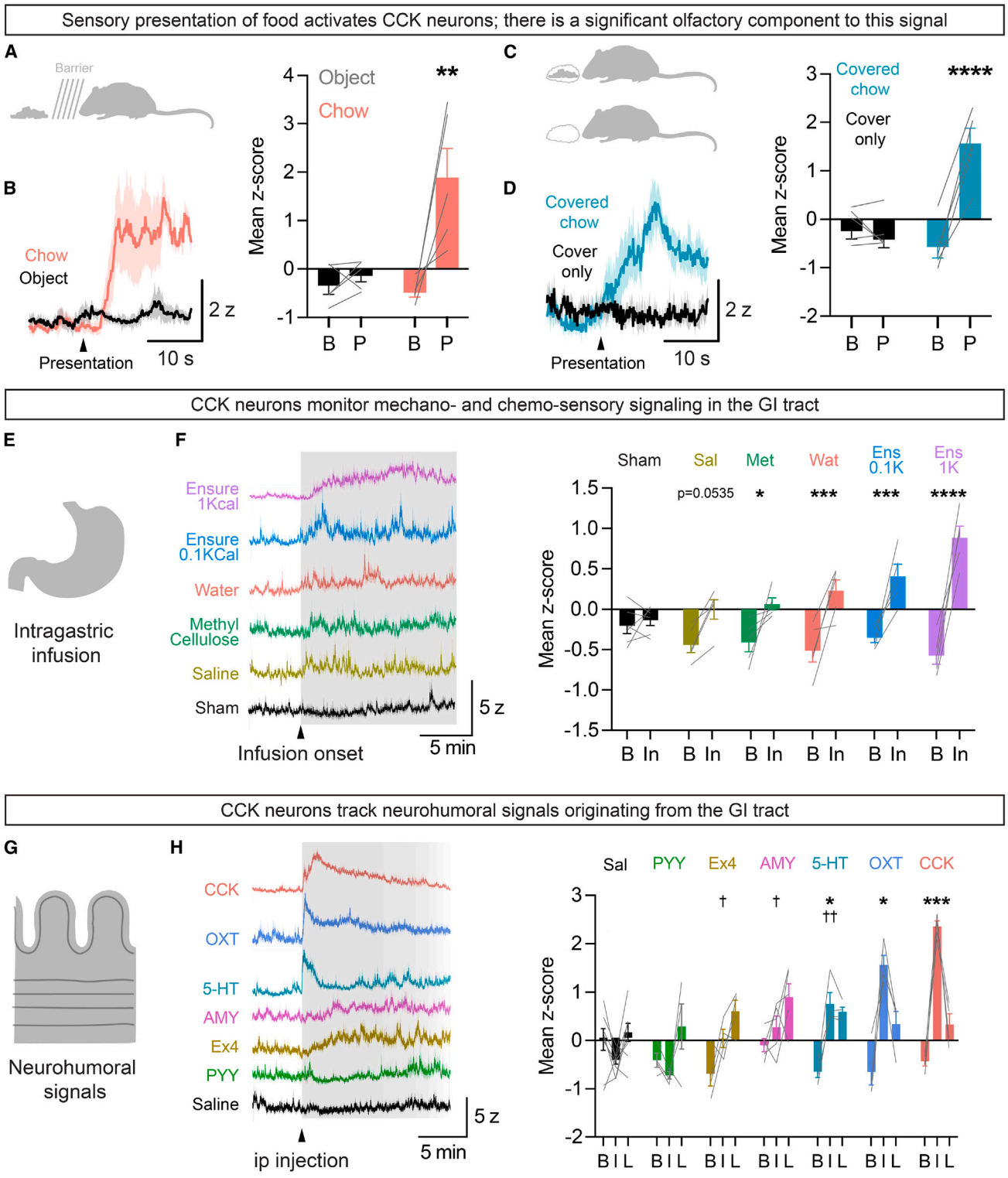

Figure 5. CCK neurons track food from sensory presentation through ingestion

(A) Schema for the sensory presentation of food.

(B) Sensory presentation of food (but not an arbitrary object) rapidly activates CCK neurons (left, averaged photometry traces; right, mean *Z* scores; *n* = 5 mice).

(C) Schema for olfactory exposure to food.

(D) Covered chow potently activates CCK neurons (left, averaged photometry traces; right, mean *Z* scores; *n* = 5 mice).

(legend continued on next page)

fully attributable to a reduction in meal size (Figure 4B). Importantly, this occurred without altering meal number (Figure 4C) or the inter-meal interval (Figure S5B), consistent with a role for these neurons in regulating satiation-related functions and not hunger or satiety.[64] These data suggest that CCK neurons track shorter- and longer-acting neurohumoral signals to specifically terminate a meal.

Meals play out over the course of much longer time scales than those observed for CCK phasic neuronal activity. One question that thus remained from these studies was how the moment-to-moment activity of CCK neurons during feeding could later lead to the termination of a meal. One mechanism consistent with our observations would be that these neurons broadcast a short-lived signal, with effects outlasting the stimulus (hysteresis), to induce delayed termination of food intake on a meal-to-meal basis. To test this hypothesis, we designed two separate assays with distinct stimulation paradigms (Figure 4D). We first performed another re-feeding assay where CCK neurons were optogenetically activated prior to access to food (pre-stimulation; Figure 4D, top). In this assay, we found that pre-stimulation of CCK neurons was able to significantly suppress food intake over the duration of an hour-long session, demonstrating that this signal is sustained (Figure 4E, left). We then asked how long this signal lasts. When we binned consumption into shorter time windows, we found that the reduction in feeding was completely accounted for within the first 30 min of the session (Figure 4E, right), and ~89% of the suppression effect was observed within the first 20 min of access to food (Figure S5C). These findings support a role for CCK neurons in broadcasting a sustained satiation signal.

In a separate study, we then performed optogenetic stimulation that was time-locked to bites of food, meant to mimic the exaggerated natural activity patterns of these neurons during feeding. In this closed-loop stimulation paradigm, we delivered 5 s pulses of light after each pellet retrieval (Figure 4D, bottom). Using this approach, we found that meal size was significantly reduced compared with controls (Figure 4F). Critically, meal termination was not immediately time-locked to the onset of laser stimulation, as the average meal size was greater than one pellet (i.e., mice do not stop consuming immediately after their first bite of food). This was also true of the first meal post-starvation (where meal sizes ranged from 2 to 13 pellets; Figure S5D). These results suggest that this anorexigenic signal has a built-in delay meant to restrain feeding through the termination of meals, and not individual bites per se. In further support of this hypothesis, we found that varying pre-stimulation times suppressed total food intake in a time-dependent manner; however, these differences were not observed at the earliest post-simulation time points (Figures S5E and S5F). Together, these results indicate that CCK neurons track food intake on a bite-to-bite basis and use this information to terminate meals through a delayed and sustained anorexigenic signal operating on the order of tens of minutes.

Our *in vivo* recordings and optical manipulations together suggested a negative feedback mechanism through which CCK neurons regulate meal termination. One key prediction of this model is that loss of negative feedback would lead to an increase in meal size. To test this hypothesis, we inhibited CCK neurons using Kir2.1[65] and performed a 1 hr fast-refeed study. Notably, this manipulation did not impact overall food intake (Figure 4G, left). However, there was a marked shift in the distribution of inter-pellet intervals (Figure 4G, right). Upon closer inspection, we found that meal size was significantly increased, as predicted by our negative feedback model (Figure 4H). This increase in meal size was compensated for by a decrease in meal frequency (Figure 4I) and a borderline increase in inter-meal interval (Figure S6A), consistent with effects seen in other populations exclusively controlling meal termination.[14] Importantly, we observed these same effects using constant optogenetic inhibition with ACR2[66] (Figures S6B–S6G). Inhibition had no impact on any other behaviors tested (Figures S6H–S6J). Our studies thus support a key role for CCK neurons in the regulation of meal size and, consequently, satiation.

Sensory detection of food via olfactory cues

Satiation-related signals arise from multiple levels of the GI tract and likely synergize with internal state and exteroceptive cues, such as the sensory presentation and taste of food.[1,18,20,67] We thus set out to investigate whether sensory variables regulate CCK neuron activity. CCK neurons are rapidly activated by feeding, and this activity precedes the first bite of food, suggesting that these neurons are capable of detecting distal cues, such as the mere presence of food. To test this, we performed fiber photometry recordings of these neurons while presenting inaccessible (caged) food to the animal (Figure 5A). Strikingly, within seconds of exposure to a familiar food source, CCK neuronal activity ramped up and remained elevated for tens of seconds (Figure 5B). These neurons did not respond to sensory presentation of an arbitrary, non-food object, demonstrating that they respond specifically to the sensory detection of food in the local environment, and not, say, surprise, unfamiliarity, or salience (Figure 5B). Given that this sensory signal is specific to food, we next asked what about food could elicit CCK neuron activity.

Mice rely heavily on smell to detect food in the environment,[68] and hunger state can in turn influence sensitivity to olfactory cues.[69,70] We thus hypothesized that CCK neurons may use

(E) Schema for intragastric infusion studies.
(F) Averaged traces (left) and mean *Z* score analyses (right) before (baseline) and during infusion. Mean *Z* scores: baseline (5 min prior to infusion) and infusion (first 15 min of infusion) (n = 5–6 mice).
(G) Schema for intraperitoneal (i.p.) injection studies.
(H) Averaged traces (left) and mean *Z* score analyses (right) demonstrate significant activation of CCK neurons in response to peripheral CCK, OXT, 5-HT, AMY, and Ex-4, but not $PYY_{3–36}$. Mean *Z* scores: baseline (5 min prior to injection), injection (first 5 min after injection), late signal (10–15 min post-injection) (n = 4–8 mice per group). † $p < 0.05$, †† $p < 0.01$ for late signal (compared with baseline).
B, baseline; I, injection; In, infusion; L, late signal; P, presentation.
*$p < 0.05$, **$p < 0.01$, ***$p < 0.001$, ****$p < 0.0001$. Data are presented as mean ± SEM.

this same sensory modality to track nutrients. To address this question, we presented mice with a pellet of food that was covered in aluminum foil (but with perforations to allow for detection of the food's scent; Figure 5C). This covered pellet was thus not directly visible to the mice and was inaccessible for consumption but could still be physically investigated. We found that immediately upon presentation of the covered food source, there was a significant elevation in CCK neuron activity (Figure 5D). Importantly, presentation of the same foil but without food enclosed had no impact on neuronal activity (Figure 5D). Together, these studies demonstrate that CCK neurons are capable of sensory detection of local food sources and that this is accomplished, at least in part, through olfactory cues.

Moment-to-moment neuronal monitoring of ingestion

But how do distal, pre-ingestive signals arise? One hypothesis is that animals learn to associate the unconditioned stimulus of nutrients in the gut with the sensory detection of food.[67,71] Given that satiation arises from a confluence of factors, including both sensory and ingestive variables, this raised the intriguing possibility that CCK neurons could integrate multiple layers of signals, including those originating from the GI tract. We thus set out to address this question by performing intragastric infusions while simultaneously monitoring CCK neuronal activity (Figure 5E).

We first took overnight-fasted mice and performed intragastric infusions of liquid nutrient (Ensure). Using this preparation, we found that direct infusion of nutrient significantly activated CCK neurons (Figure 5F). These effects were slow in onset, taking about 1–2 min prior to a ramp-up in activity, followed by a peak in activity around 10 min into the infusion. These results also held for a less concentrated infusion of Ensure, albeit with a smaller magnitude of effect (Figure 5F). We next asked whether this signal could be attributed to gut mechano- and/or chemosensation. We tested a variety of non-nutritive stimuli, including solutions of different viscosity and/or osmolarity that are absorbed (water and saline) or not absorbed (methylcellulose). All non-nutritive stimuli tested significantly activated CCK neurons with approximately the same magnitude of effect, though the response was markedly weaker compared with that elicited by Ensure (Figure 5F). Together, these results suggest that these neurons synergistically respond to gut mechano- and chemosensory cues.

We next asked whether these neurons are also responsive to gut-derived signals naturally released in response to ingestion. We addressed this question by recording from CCK neurons while manipulating key signaling pathways that act across the upper GI tract (Figure 5G). We thus intraperitoneally injected CCK, exendin-4 (Ex4, an agonist of the glucagon-like peptide-1 receptor), peptide $YY_{3–36}$ ($PYY_{3–36}$, an agonist of the neuropeptide Y receptor Y2), serotonin (5-HT), oxytocin (OXT), or amylin (AMY). We found that each of these compounds, with the exception of $PYY_{3–36}$, significantly activated CCK neurons with distinct kinetics (Figure 5H). Both CCK and OXT elicited rapid and sustained signals that persisted for ~10 min; 5-HT had a biphasic signal, comprised of an initial rapid activation, followed by a lower-amplitude signal persisting for minutes; and AMY and Ex4 injections both led to slow but significant rises in activity that persisted for most of the recording session.

Together, our data demonstrate that CCK neurons track ingestion and monitor its consequences through the detection of key neurohumoral cues, possibly through vagal-mediated signals.[13] Notably, many of these effects are likely to be mediated by polysynaptic neuronal relays, as opposed to humoral signaling, given their rapidity and our inability to significantly enrich for these peptides' key receptors in CCK neurons (Table S2). We next set out to determine the input-output architecture of CCK neurons.

Wiring features of a satiation center

To identify the loci that provide direct input onto CCK neurons, we performed monosynaptic tracing[72–74] (Figures 6A and 6B). Despite being a relatively small population of cells, CCK neurons received substantial inputs from structures across the brain. Consistent with their responses to diverse cognitive, sensory, and neurohumoral signals, these neurons received inputs covering loci from forebrain to midbrain and hindbrain (Figures 6C and 6D). Across the forebrain, many labeled structures are known to regulate feeding. Prominent inputs, for example, were observed from the central amygdala (CeA) and the bed nucleus of the stria terminalis (BNST). The hypothalamus also provided substantial inputs and accounted for ~20% of cells innervating CCK neurons, with major contributions from the lateral hypothalamus (LH) and zona incerta.

The primary contribution to CCK neurons came from the brainstem, accounting for ~57% of total inputs. Several midbrain and hindbrain structures, including those that are integrated into the basal ganglia and important for goal-directed behaviors, innervated CCK neurons. These included the ventral tegmental area, substantia nigra, laterodorsal tegmental nucleus, and pedunculopontine tegmental nucleus. CCK neurons also received ascending inputs from across the hindbrain (Figures 6C and 6D). A number of these loci, including the PBN and NTS, are known to play key roles in visceral sensation/interoception and consequently impact multiple aspects of feeding.

To better understand how these neurons function at the circuit level, we next asked where they project. We mapped CCK neuronal projection targets by simultaneously labeling axons and nerve terminals (Figures 6E and 6F). Somewhat surprisingly, these neurons projected to very few targets (Figures 6G and 6H). In the forebrain, this included the BNST, CeA, and LH, as well as dorsal tenia tecta, striatum, lateral septum, and the posterior segment of the basolateral amygdala. In the hindbrain, these neurons selectively targeted the peri-locus coeruleus. We next confirmed a functional connection between CCK neurons and these targets, performing whole-brain Fos mapping after activating CCK neurons (Figures S7A and S7B). This showed broad activation across the forebrain, midbrain, and hindbrain, including most of the structures monosynaptically downstream of CCK neurons. Together, these results propose a circuit logic (Figure 7A) and negative feedback mechanism (Figure 7B) through which CCK neurons sense and respond to diverse signals to regulate meal size.

DISCUSSION

Satiation drives meal termination and is thus a key determinant of energy balance. Since the work of Grill and Norgren in the 1970s,

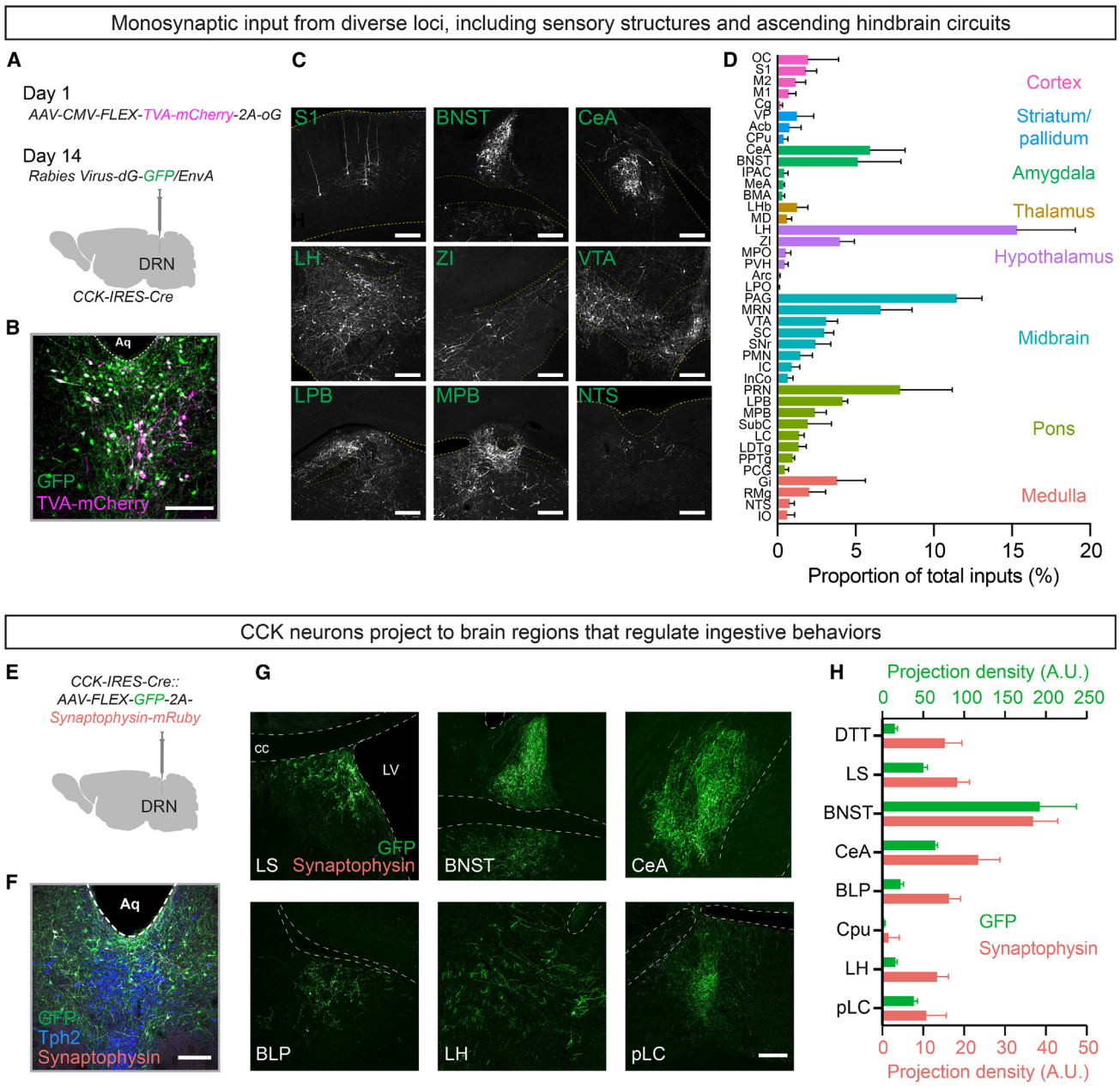

Figure 6. CCK neurons receive monosynaptic inputs from across the brain and project to limited targets

(A) Schema for rabies tracing.
(B) Starter cells in DRN.
(C) Representative images of inputs along the brain's anterior-posterior axis.
(D) Quantification of inputs to CCK neurons (n = 3 mice).
(E) Schema for anterograde projection mapping using a dual-reporter construct.
(F) CCK cells are labeled with GFP and mRuby but do not overlap with Tph2 expression.
(G) Representative images demonstrate a restricted set of projections to the forebrain and hindbrain.
(H) Quantification of CCK neuron projections (n = 4 mice).
Anatomic abbreviations can be found in STAR Methods. Scale bars, 200 μm. a.u., arbitrary units. Data are presented as mean ± SEM.
See also Figure S7.

neurons regulating satiation have been localized to the brainstem, yet the specific location and identity of these neurons have remained unknown.[7] Here, we used spatially resolved molecular profiling[39,40] (Figure 1) to identify CCK-expressing neurons of the DRN as key regulators of satiation (Figures 2 and 4). These CCK neurons monitor consumption on a bite-to-bite basis and

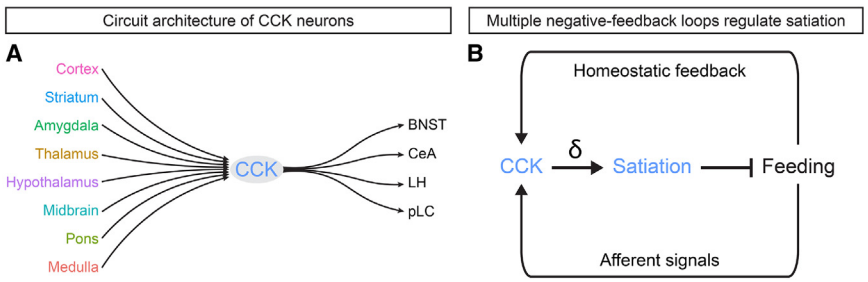

Figure 7. Structural and functional features of CCK neurons

(A) CCK neurons are integrated into the extended circuitry known to regulate feeding.

(B) CCK neurons regulate satiation through multiple negative feedback loops. These neurons broadcast a sustained signal with a built-in delay (δ) and are regulated by both homeostatic and afferent cues.

can use this information to passively encode a meal (Figure 3). They are also able to track food from its sensory presentation through its ingestion (Figure 5) and consequently suppress feeding through a short-lived yet hysteretic signal that ultimately results in meal termination (Figure 4). Consistent with their key role in satiation, CCK neurons are also molecularly (Figure 2) and anatomically (Figure 6) well positioned to receive diverse lines of cognitive and sensory information. Together, these studies reveal important principles through which the brainstem regulates satiation and begin to shed light on the neural determinants of meal size (Figure 7).

We believe that the present work, in aggregate, makes three important advances. We find that (1) CCK neurons track diverse neurohormonal cues to signal food intake on a bite-to-bite basis and that this allows for the passive encoding of meal size, (2) these neurons transform this information into a sustained signal with a built-in delay to ultimately terminate a meal, and (3) CCK neurons are positioned at the intersection of multiple negative feedback loops critical for the integrative control of satiation. This work raises fundamental questions about how the brain is wired to terminate a meal and, beyond that, how innate, recurring behaviors are regulated.

Ingestive variables encoded by brainstem satiation neurons

One open question in neuroscience is how parameters for survival-related functions, such as energy homeostasis, are set (if at all) and tuned. Since all living organisms need to acquire energy to survive, food intake offers a unique lens through which we can understand defended variables and, consequently, evolutionarily conserved neural functioning. Under the umbrella of food intake, meal size is a discrete parameter that is well defined but with biological underpinnings that are poorly understood. In this work, we leverage a previously uncharacterized brainstem peptidergic cell type to better understand the neural regulation of meal size and use this to gain further insight into how satiation works.

Meal size and timing arise from a confluence of factors, including internal state, external environmental conditions, and their interplay. Meal termination is a decision, one where the evidence is comprised of many sensory variables (taste, texture, GI chemo- and mechanosensation) that play out on a background of internal states (e.g., hunger and arousal), as well as ambient (e.g., food availability and proximity) and internal conditions (e.g., volume status, core temperature, and available energy stores). We find that CCK neurons represent the cellular implementation of a sense-and-respond system where food intake is tracked and transformed into the decision to terminate a meal.

With the initial discovery of satiation factors,[50] Gibbs and Smith proposed five criteria through which a humoral factor could be considered a negative regulator of meal size. These criteria, which also hold well for cell types proposed to regulate satiation (placed in parentheses), require that this factor (neuron) (1) is released (activated) naturalistically during feeding, (2) can suppress feeding in a scalable manner after external administration (stimulation), (3) has a short onset and duration of action, (4) does not cause illness, and (5) exerts its effects when administered (stimulated) at physiological doses.[1,50] We believe that CCK neurons satisfy many, if not all, of these criteria, positioning them as key regulators of satiation. While a number of other cell types have recently been shown to play a similar role in the short-term regulation of meal size,[15,18] these same cell types do not appear to integrate such diverse (yet feeding-relevant) signals as CCK neurons. Our neuroanatomic studies begin to shed light on how these neurons are so well attuned to key sensory and neurohumoral variables relevant to meal size and timing.

Given decades of work on the input/output architecture of the DRN,[26,75] it is somewhat surprising that a role for the DRN in meal size had not been appreciated earlier. The DRN is known to receive convergent inputs from across the brain, including many of the key loci involved in acute and chronic regulation of food intake and body weight.[28,34,76] However, the DRN is also molecularly heterogeneous, with intermingled cell types often playing opposing roles in feeding,[36] and this likely stymied earlier efforts to uncover specific roles for the area's component cell types. With the recent application of single-cell-resolved sequencing methods to the DRN,[45] this problem has become more tractable.[77] In our spatially resolved, single-cell profiling studies, we found a high degree of agreement with published work,[45] while also uncovering a previously underappreciated peptidergic population that exists outside of the nearby Edinger-Westphal nucleus. Our results thus propose an obligate peptidergic cell type residing within the DRN and further underscore the power of using spatially resolved methods for molecular profiling.

A latent role for neuropeptide signaling in acute behavioral control

How might this peptidergic character begin to explain the integrative function of CCK neurons? Our studies present a working model in which acute changes in somatic neuronal activity are "built up" (integrated) at a downstream site, and this results in

brief yet significant changes in feeding microstructure. These changes are brought about through a signal that is relatively short-lived, operating on the order of tens of minutes, and has a built-in delay. Neuromodulatory signaling is ideally suited to these computational functions, which link short-term neuronal activity with longer-term behavioral consequences.[78]

Evidence for mechanisms of this kind has been identified across species in neural systems using neuropeptide/neuromodulator signaling[79–81] but has only recently become more appreciated within the acute context of mammalian feeding.[82,83] The fact that CCK neurons co-express many different neuropeptides suggests that there is a significant level of redundancy in this system. Given that many of the same peptides (or peptide systems) seen in CCK neurons are also found across the evolutionary spectrum in cell types with similar functions (including *Drosophila*[84,85]), one intriguing hypothesis is that these neurons use conserved molecular, cellular, and/or circuit mechanisms to drive acute changes in behavior. By studying satiation through the lens of CCK neurons, the present work thus opens up avenues for understanding the central regulation of feeding and proposes a key entry point for studying neuromodulatory function.

Limitations of the study

Two important questions remain from this work: (1) how do these neurons receive and integrate diverse streams of neurohormonal signaling? And (2) how do CCK neurons induce their characteristic, sustained satiation signals? Additional structural and functional studies will be required to parse out the long-range inputs converging on these neurons, which convey both sensory and cognitive lines of information. Analysis of population and subcellular molecular signaling will also likely be critical in revealing the nature of the leaky integrator-like properties exhibited by CCK neurons. Furthermore, functional studies probing the molecular composition of CCK neurons will begin to uncover the mechanisms governing sustained satiation signaling.

RESOURCE AVAILABILITY

Lead contact

Requests for further information and resources should be directed to and will be fulfilled by the lead contact, Alexander Nectow (arn2136@columbia.edu).

Materials availability

This study did not generate new, unique reagents.

Data and code availability

Sequencing data were deposited as follows: vTRAP (GEO: GSE252409), STARmap/RIBOmap (Zenodo: https://doi.org/10.5281/zenodo.14447775). Code was deposited to GitHub (https://github.com/wanglab-broad/drn-analysis). All data and code are publicly available as of the date of publication.

ACKNOWLEDGMENTS

The authors thank Gary Schwartz, Mike Crickmore, and Stephen Zhang for helpful discussions and the following individuals for technical input: Johannes de Jong, Stephan Lammel, Akeem Pinnock, Anthony Ferrante, Alexxai Kravitz, Xin Sui, Zefang Tang, Yichun He, Hailing Shi, Simoni Tiano, and the Columbia Genome Center. Some figures were made using BioRender. HSV and rabies constructs were obtained from CNNV (P40-OD010996). S.C. is supported by the Russell Berrie Foundation Fellowship and the American Diabetes Association. W.X.W. is supported by the Damon Runyon Cancer Research Foundation's Damon Runyon-National Mah Jongg League, Inc. Fellowship. X.W. acknowledges support from Searle Scholars, Thomas D. and Virginia W. Cabot and Edward Scolnick Professorships, an Ono Pharma Breakthrough Science Initiative Award, Merkin Institute Fellowship, and an NIH New Innovator Award. A.R.N acknowledges support from the American Diabetes Association (Pathway to Stop Diabetes and Core programs), the New York Obesity (P30DK026687) and Diabetes (P30DK063608) Research Centers, and the Berrie Program in the Neurobiology of Body Weight Regulation. A.R.N. also acknowledges generous support from Donald Landry as well as Ali Gharavi, Anthony Ferrante, and Allan Schwartz.

AUTHOR CONTRIBUTIONS

S.C. and A.R.N. conceived and designed the research study. S.C., N.G.K., and W.X.W. performed the experiments with assistance from C.A.A., A.N., V.M.B., and C.M.K. H.H. provided key viral reagents. S.C., N.G.K., W.X.W., J.H., J.W., X.W., and A.R.N. performed data analysis. A.R.N. secured funding. A.R.N. and X.W. supervised the work. S.C. and A.R.N. wrote the manuscript with input from all authors.

DECLARATION OF INTERESTS

X.W. is a co-founder of Stellaromics, Inc.

STAR★METHODS

Detailed methods are provided in the online version of this paper and include the following:

- KEY RESOURCES TABLE
- EXPERIMENTAL MODEL AND STUDY PARTICIPANT DETAILS
  - Mice
- METHOD DETAILS
  - STARmap/RIBOmap protocol
  - Sample preparation
  - Library construction
  - *In situ* sequencing
  - STARmap and RIBOmap Data Analysis
  - Image pre-processing
  - Cell segmentation
  - Quality control for cells
  - Cell type annotations for full dataset
  - Cell type annotations for DRN neurons
  - Subclustering analysis of TH neurons
  - Single molecule fluorescence *in situ* hybridization (smFISH)
  - Molecular profiling using vTRAP
  - Intracranial viral injections and fiber optic implantations
  - Gastric catheter implantation surgeries
  - Fos labeling
  - Optogenetic stimulation
  - Behavioral studies
  - Feeding and drinking assays
  - Meal pattern analysis using FED3 devices
  - Closed-loop optogenetic experiments
  - Open field test (OFT)
  - Real-time place preference (RTPP)
  - Intragastric infusion (IGI) studies
  - Fiber photometry recording and data analysis
  - Monosynaptic viral tracing using rabies virus
  - Anterograde viral tracing
  - Whole-brain Fos mapping
  - Histology
- QUANTIFICATION AND STATISTICAL ANALYSIS

SUPPLEMENTAL INFORMATION

Supplemental information can be found online at https://doi.org/10.1016/j.cell.2025.01.018.

Received: February 16, 2024
Revised: December 3, 2024
Accepted: January 10, 2025
Published: February 5, 2025

REFERENCES

1. Smith, G.P. (1998). Satiation: from Gut to Brain (Oxford University Press).
2. Cummings, D.E., and Overduin, J. (2007). Gastrointestinal regulation of food intake. J. Clin. Invest. *117*, 13–23. https://doi.org/10.1172/JCI30227.
3. Watts, A.G., Kanoski, S.E., Sanchez-Watts, G., and Langhans, W. (2022). The physiological control of eating: signals, neurons, and networks. Physiol. Rev. *102*, 689–813. https://doi.org/10.1152/physrev.00028.2020.
4. Andermann, M.L., and Lowell, B.B. (2017). Toward a Wiring Diagram Understanding of Appetite Control. Neuron *95*, 757–778. https://doi.org/10.1016/j.neuron.2017.06.014.
5. Hetherington, A.W., and Ranson, S.W. (1940). Hypothalamic lesions and adiposity in the rat. Anat. Rec. *78*, 149–172. https://doi.org/10.1002/ar.1090780203.
6. Delgado, J.M., and Anand, B.K. (1953). Increase of food intake induced by electrical stimulation of the lateral hypothalamus. Am. J. Physiol. *172*, 162–168. https://doi.org/10.1152/ajplegacy.1952.172.1.162.
7. Grill, H.J., and Norgren, R. (1978). Chronically decerebrate rats demonstrate satiation but not bait shyness. Science *201*, 267–269. https://doi.org/10.1126/science.663655.
8. Seeley, R.J., Grill, H.J., and Kaplan, J.M. (1994). Neurological dissociation of gastrointestinal and metabolic contributions to meal size control. Behav. Neurosci. *108*, 347–352. https://doi.org/10.1037/0735-7044.108.2.347.
9. Grill, H.J., and Hayes, M.R. (2012). Hindbrain neurons as an essential hub in the neuroanatomically distributed control of energy balance. Cell Metab. *16*, 296–309. https://doi.org/10.1016/j.cmet.2012.06.015.
10. Grill, H.J., and Kaplan, J.M. (1992). Sham feeding in intact and chronic decerebrate rats. Am. J. Physiol. *262*, R1070–R1074. https://doi.org/10.1152/ajpregu.1992.262.6.R1070.
11. Hayes, M.R., Skibicka, K.P., and Grill, H.J. (2008). Caudal brainstem processing is sufficient for behavioral, sympathetic, and parasympathetic responses driven by peripheral and hindbrain glucagon-like-peptide-1 receptor stimulation. Endocrinology *149*, 4059–4068. https://doi.org/10.1210/en.2007-1743.
12. Grill, H.J., and Smith, G.P. (1988). Cholecystokinin decreases sucrose intake in chronic decerebrate rats. Am. J. Physiol. *254*, R853–R856. https://doi.org/10.1152/ajpregu.1988.254.6.R853.
13. Berthoud, H.R., Albaugh, V.L., and Neuhuber, W.L. (2021). Gut-brain communication and obesity: understanding functions of the vagus nerve. J. Clin. Invest. *131*, e143770. https://doi.org/10.1172/JCI143770.
14. Campos, C.A., Bowen, A.J., Schwartz, M.W., and Palmiter, R.D. (2016). Parabrachial CGRP Neurons Control Meal Termination. Cell Metab. *23*, 811–820. https://doi.org/10.1016/j.cmet.2016.04.006.
15. Cheng, W., Gordian, D., Ludwig, M.Q., Pers, T.H., Seeley, R.J., and Myers, M.G., Jr. (2022). Hindbrain circuits in the control of eating behaviour and energy balance. Nat. Metab. *4*, 826–835. https://doi.org/10.1038/s42255-022-00606-9.
16. Campos, C.A., Bowen, A.J., Roman, C.W., and Palmiter, R.D. (2018). Encoding of danger by parabrachial CGRP neurons. Nature *555*, 617–622. https://doi.org/10.1038/nature25511.
17. Palmiter, R.D. (2018). The Parabrachial Nucleus: CGRP Neurons Function as a General Alarm. Trends Neurosci. *41*, 280–293. https://doi.org/10.1016/j.tins.2018.03.007.
18. Ly, T., Oh, J.Y., Sivakumar, N., Shehata, S., La Santa Medina, N., Huang, H., Liu, Z., Fang, W., Barnes, C., Dundar, N., et al. (2023). Sequential appetite suppression by oral and visceral feedback to the brainstem. Nature *624*, 130–137. https://doi.org/10.1038/s41586-023-06758-2.
19. Ludwig, M.Q., Cheng, W., Gordian, D., Lee, J., Paulsen, S.J., Hansen, S.N., Egerod, K.L., Barkholt, P., Rhodes, C.J., Secher, A., et al. (2021). A genetic map of the mouse dorsal vagal complex and its role in obesity. Nat. Metab. *3*, 530–545. https://doi.org/10.1038/s42255-021-00363-1.
20. Smith, G.P. (1996). The direct and indirect controls of meal size. Neurosci. Biobehav. Rev. *20*, 41–46. https://doi.org/10.1016/0149-7634(95)00038-g.
21. Huang, D., Grady, F.S., Peltekian, L., and Geerling, J.C. (2021). Efferent projections of Vglut2, Foxp2, and Pdyn parabrachial neurons in mice. J. Comp. Neurol. *529*, 657–693. https://doi.org/10.1002/cne.24975.
22. Huang, D., Grady, F.S., Peltekian, L., Laing, J.J., and Geerling, J.C. (2021). Efferent projections of CGRP/Calca-expressing parabrachial neurons in mice. J. Comp. Neurol. *529*, 2911–2957. https://doi.org/10.1002/cne.25136.
23. Geerling, J.C., and Loewy, A.D. (2006). Aldosterone-sensitive neurons in the nucleus of the solitary: efferent projections. J. Comp. Neurol. *498*, 223–250. https://doi.org/10.1002/cne.20993.
24. Herbert, H., and Saper, C.B. (1992). Organization of medullary adrenergic and noradrenergic projections to the periaqueductal gray matter in the rat. J. Comp. Neurol. *315*, 34–52. https://doi.org/10.1002/cne.903150104.
25. Han, W., Tellez, L.A., Perkins, M.H., Perez, I.O., Qu, T., Ferreira, J., Ferreira, T.L., Quinn, D., Liu, Z.W., Gao, X.B., et al. (2018). A Neural Circuit for Gut-Induced Reward. Cell *175*, 887–888. https://doi.org/10.1016/j.cell.2018.10.018.
26. Weissbourd, B., Ren, J., DeLoach, K.E., Guenthner, C.J., Miyamichi, K., and Luo, L. (2014). Presynaptic partners of dorsal raphe serotonergic and GABAergic neurons. Neuron *83*, 645–662. https://doi.org/10.1016/j.neuron.2014.06.024.
27. Pollak Dorocic, I., Fürth, D., Xuan, Y., Johansson, Y., Pozzi, L., Silberberg, G., Carlén, M., and Meletis, K. (2014). A whole-brain atlas of inputs to serotonergic neurons of the dorsal and median raphe nuclei. Neuron *83*, 663–678. https://doi.org/10.1016/j.neuron.2014.07.002.
28. Stachniak, T.J., Ghosh, A., and Sternson, S.M. (2014). Chemogenetic synaptic silencing of neural circuits localizes a hypothalamus →midbrain pathway for feeding behavior. Neuron *82*, 797–808. https://doi.org/10.1016/j.neuron.2014.04.008.
29. Geerling, J.C., Shin, J.W., Chimenti, P.C., and Loewy, A.D. (2010). Paraventricular hypothalamic nucleus: axonal projections to the brainstem. J. Comp. Neurol. *518*, 1460–1499. https://doi.org/10.1002/cne.22283.
30. Currie, P.J., Fletcher, P.J., and Coscina, D.V. (1994). Administration of 8-OH-DPAT into the midbrain raphe nuclei: effects on medial hypothalamic NE-induced feeding. Am. J. Physiol. *266*, R1645–R1651. https://doi.org/10.1152/ajpregu.1994.266.5.R1645.
31. Przewłocka, B., Stala, L., and Scheel-Krüger, J. (1979). Evidence that GABA in the nucleus dorsalis raphe induces stimulation of locomotor activity and eating behavior. Life Sci. *25*, 937–945. https://doi.org/10.1016/0024-3205(79)90499-5.
32. Klitenick, M.A., and Wirtshafter, D. (1988). Comparative studies of the ingestive behaviors produced by microinjections of muscimol into the midbrain raphe nuclei of the ventral tegmental area of the rat. Life Sci. *42*, 775–782. https://doi.org/10.1016/0024-3205(88)90650-9.
33. Jenck, F., Quirion, R., and Wise, R.A. (1987). Opioid receptor subtypes associated with ventral tegmental facilitation and periaqueductal gray inhibition of feeding. Brain Res. *423*, 39–44. https://doi.org/10.1016/0006-8993(87)90822-5.
34. Bhave, V.M., and Nectow, A.R. (2021). The dorsal raphe nucleus in the control of energy balance. Trends Neurosci. *44*, 946–960. https://doi.org/10.1016/j.tins.2021.09.004.
35. Schneeberger, M., Parolari, L., Das Banerjee, T., Bhave, V., Wang, P., Patel, B., Topilko, T., Wu, Z., Choi, C.H.J., Yu, X., et al. (2019). Regulation of Energy Expenditure by Brainstem GABA Neurons. Cell *178*, 672–685.e12. https://doi.org/10.1016/j.cell.2019.05.048.
36. Nectow, A.R., Schneeberger, M., Zhang, H., Field, B.C., Renier, N., Azevedo, E., Patel, B., Liang, Y., Mitra, S., Tessier-Lavigne, M., et al. (2017).

Identification of a Brainstem Circuit Controlling Feeding. Cell *170*, 429–442.e11. https://doi.org/10.1016/j.cell.2017.06.045.

37. Hao, S., Yang, H., Wang, X., He, Y., Xu, H., Wu, X., Pan, L., Liu, Y., Lou, H., Xu, H., et al. (2019). The Lateral Hypothalamic and BNST GABAergic Projections to the Anterior Ventrolateral Periaqueductal Gray Regulate Feeding. Cell Rep. *28*, 616–624.e5. https://doi.org/10.1016/j.celrep.2019.06.051.
38. Li, M.M., Madara, J.C., Steger, J.S., Krashes, M.J., Balthasar, N., Campbell, J.N., Resch, J.M., Conley, N.J., Garfield, A.S., and Lowell, B.B. (2019). The Paraventricular Hypothalamus Regulates Satiety and Prevents Obesity via Two Genetically Distinct Circuits. Neuron *102*, 653–667.e6. https://doi.org/10.1016/j.neuron.2019.02.028.
39. Wang, X., Allen, W.E., Wright, M.A., Sylwestrak, E.L., Samusik, N., Vesuna, S., Evans, K., Liu, C., Ramakrishnan, C., Liu, J., et al. (2018). Three-dimensional intact-tissue sequencing of single-cell transcriptional states. Science *361*, eaat5691. https://doi.org/10.1126/science.aat5691.
40. Zeng, H., Huang, J., Ren, J., Wang, C.K., Tang, Z., Zhou, H., Zhou, Y., Shi, H., Aditham, A., Sui, X., et al. (2023). Spatially resolved single-cell translatomics at molecular resolution. Science *380*, eadd3067. https://doi.org/10.1126/science.add3067.
41. Ren, J., Isakova, A., Friedmann, D., Zeng, J., Grutzner, S.M., Pun, A., Zhao, G.Q., Kolluru, S.S., Wang, R., Lin, R., et al. (2019). Single-cell transcriptomes and whole-brain projections of serotonin neurons in the mouse dorsal and median raphe nuclei. eLife *8*, e49424. https://doi.org/10.7554/eLife.49424.
42. Okaty, B.W., Sturrock, N., Escobedo Lozoya, Y., Chang, Y., Senft, R.A., Lyon, K.A., Alekseyenko, O.V., and Dymecki, S.M. (2020). A single-cell transcriptomic and anatomic atlas of mouse dorsal raphe Pet1 neurons. eLife *9*, e55523. https://doi.org/10.7554/eLife.55523.
43. Korsunsky, I., Millard, N., Fan, J., Slowikowski, K., Zhang, F., Wei, K., Baglaenko, Y., Brenner, M., Loh, P.R., and Raychaudhuri, S. (2019). Fast, sensitive and accurate integration of single-cell data with Harmony. Nat. Methods *16*, 1289–1296. https://doi.org/10.1038/s41592-019-0619-0.
44. Shi, H., He, Y., Zhou, Y., Huang, J., Maher, K., Wang, B., Tang, Z., Luo, S., Tan, P., Wu, M., et al. (2023). Spatial atlas of the mouse central nervous system at molecular resolution. Nature *622*, 552–561. https://doi.org/10.1038/s41586-023-06569-5.
45. Huang, K.W., Ochandarena, N.E., Philson, A.C., Hyun, M., Birnbaum, J.E., Cicconet, M., and Sabatini, B.L. (2019). Molecular and anatomical organization of the dorsal raphe nucleus. eLife *8*, e46464. https://doi.org/10.7554/eLife.46464.
46. Lein, E.S., Hawrylycz, M.J., Ao, N., Ayres, M., Bensinger, A., Bernard, A., Boe, A.F., Boguski, M.S., Brockway, K.S., Byrnes, E.J., et al. (2007). Genome-wide atlas of gene expression in the adult mouse brain. Nature *445*, 168–176. https://doi.org/10.1038/nature05453.
47. Okaty, B.W., Freret, M.E., Rood, B.D., Brust, R.D., Hennessy, M.L., deBairos, D., Kim, J.C., Cook, M.N., and Dymecki, S.M. (2015). Multi-Scale Molecular Deconstruction of the Serotonin Neuron System. Neuron *88*, 774–791. https://doi.org/10.1016/j.neuron.2015.10.007.
48. Roman, C.W., Sloat, S.R., and Palmiter, R.D. (2017). A tale of two circuits: CCK^{NTS} neuron stimulation controls appetite and induces opposing motivational states by projections to distinct brain regions. Neuroscience *358*, 316–324. https://doi.org/10.1016/j.neuroscience.2017.06.049.
49. D'Agostino, G., Lyons, D.J., Cristiano, C., Burke, L.K., Madara, J.C., Campbell, J.N., Garcia, A.P., Land, B.B., Lowell, B.B., Dileone, R.J., et al. (2016). Appetite controlled by a cholecystokinin nucleus of the solitary tract to hypothalamus neurocircuit. eLife *5*, e12225. https://doi.org/10.7554/eLife.12225.
50. Gibbs, J., Young, R.C., and Smith, G.P. (1973). Cholecystokinin decreases food intake in rats. J. Comp. Physiol. Psychol. *84*, 488–495. https://doi.org/10.1037/h0034870.
51. Nectow, A.R., Moya, M.V., Ekstrand, M.I., Mousa, A., McGuire, K.L., Sferrazza, C.E., Field, B.C., Rabinowitz, G.S., Sawicka, K., Liang, Y., et al. (2017). Rapid Molecular Profiling of Defined Cell Types Using Viral TRAP. Cell Rep. *19*, 655–667. https://doi.org/10.1016/j.celrep.2017.03.048.
52. Ekstrand, M.I., Nectow, A.R., Knight, Z.A., Latcha, K.N., Pomeranz, L.E., and Friedman, J.M. (2014). Molecular profiling of neurons based on connectivity. Cell *157*, 1230–1242. https://doi.org/10.1016/j.cell.2014.03.059.
53. Nectow, A.R., Ekstrand, M.I., and Friedman, J.M. (2015). Molecular characterization of neuronal cell types based on patterns of projection with Retro-TRAP. Nat. Protoc. *10*, 1319–1327. https://doi.org/10.1038/nprot.2015.087.
54. Aitken, C.E., and Lorsch, J.R. (2012). A mechanistic overview of translation initiation in eukaryotes. Nat. Struct. Mol. Biol. *19*, 568–576. https://doi.org/10.1038/nsmb.2303.
55. Ingolia, N.T., Brar, G.A., Stern-Ginossar, N., Harris, M.S., Talhouarne, G.J.S., Jackson, S.E., Wills, M.R., and Weissman, J.S. (2014). Ribosome profiling reveals pervasive translation outside of annotated protein-coding genes. Cell Rep. *8*, 1365–1379. https://doi.org/10.1016/j.celrep.2014.07.045.
56. Tritsch, N.X., Oh, W.J., Gu, C., and Sabatini, B.L. (2014). Midbrain dopamine neurons sustain inhibitory transmission using plasma membrane uptake of GABA, not synthesis. eLife *3*, e01936. https://doi.org/10.7554/eLife.01936.
57. Tritsch, N.X., Ding, J.B., and Sabatini, B.L. (2012). Dopaminergic neurons inhibit striatal output through non-canonical release of GABA. Nature *490*, 262–266. https://doi.org/10.1038/nature11466.
58. Kim, J.I., Ganesan, S., Luo, S.X., Wu, Y.W., Park, E., Huang, E.J., Chen, L., and Ding, J.B. (2015). Aldehyde dehydrogenase 1a1 mediates a GABA synthesis pathway in midbrain dopaminergic neurons. Science *350*, 102–106. https://doi.org/10.1126/science.aac4690.
59. Ge, S.X., Jung, D., and Yao, R. (2020). ShinyGO: a graphical gene-set enrichment tool for animals and plants. Bioinformatics *36*, 2628–2629. https://doi.org/10.1093/bioinformatics/btz931.
60. Boyden, E.S., Zhang, F., Bamberg, E., Nagel, G., and Deisseroth, K. (2005). Millisecond-timescale, genetically targeted optical control of neural activity. Nat. Neurosci. *8*, 1263–1268. https://doi.org/10.1038/nn1525.
61. Kim, C.K., Yang, S.J., Pichamoorthy, N., Young, N.P., Kauvar, I., Jennings, J.H., Lerner, T.N., Berndt, A., Lee, S.Y., Ramakrishnan, C., et al. (2016). Simultaneous fast measurement of circuit dynamics at multiple sites across the mammalian brain. Nat. Methods *13*, 325–328. https://doi.org/10.1038/nmeth.3770.
62. Matikainen-Ankney, B.A., Earnest, T., Ali, M., Casey, E., Wang, J.G., Sutton, A.K., Legaria, A.A., Barclay, K.M., Murdaugh, L.B., Norris, M.R., et al. (2021). An open-source device for measuring food intake and operant behavior in rodent home-cages. eLife *10*, e66173. https://doi.org/10.7554/eLife.66173.
63. Brobeck, J.R. (1955). Neural regulation of food intake. Ann. N. Y. Acad. Sci. *63*, 44–55. https://doi.org/10.1111/j.1749-6632.1955.tb36544.x.
64. Le Magnen, J. (1985). Hunger (Cambridge University Press).
65. Beier, K.T., Kim, C.K., Hoerbelt, P., Hung, L.W., Heifets, B.D., DeLoach, K.E., Mosca, T.J., Neuner, S., Deisseroth, K., Luo, L., et al. (2017). Rabies screen reveals GPe control of cocaine-triggered plasticity. Nature *549*, 345–350. https://doi.org/10.1038/nature23888.
66. Govorunova, E.G., Sineshchekov, O.A., Janz, R., Liu, X., and Spudich, J.L. (2015). NEUROSCIENCE. Natural light-gated anion channels: A family of microbial rhodopsins for advanced optogenetics. Science *349*, 647–650. https://doi.org/10.1126/science.aaa7484.
67. Su, Z., Alhadeff, A.L., and Betley, J.N. (2017). Nutritive, Post-ingestive Signals Are the Primary Regulators of AgRP Neuron Activity. Cell Rep. *21*, 2724–2736. https://doi.org/10.1016/j.celrep.2017.11.036.
68. Fine, L.G., and Riera, C.E. (2019). Sense of Smell as the Central Driver of Pavlovian Appetite Behavior in Mammals. Front. Physiol. *10*, 1151. https://doi.org/10.3389/fphys.2019.01151.

69. Horio, N., and Liberles, S.D. (2021). Hunger enhances food-odour attraction through a neuropeptide Y spotlight. Nature *592*, 262–266. https://doi.org/10.1038/s41586-021-03299-4.

70. Root, C.M., Ko, K.I., Jafari, A., and Wang, J.W. (2011). Presynaptic facilitation by neuropeptide signaling mediates odor-driven food search. Cell *145*, 133–144. https://doi.org/10.1016/j.cell.2011.02.008.

71. Beutler, L.R., Chen, Y., Ahn, J.S., Lin, Y.C., Essner, R.A., and Knight, Z.A. (2017). Dynamics of Gut-Brain Communication Underlying Hunger. Neuron *96*, 461–475.e5. https://doi.org/10.1016/j.neuron.2017.09.043.

72. Reardon, T.R., Murray, A.J., Turi, G.F., Wirblich, C., Croce, K.R., Schnell, M.J., Jessell, T.M., and Losonczy, A. (2016). Rabies Virus CVS-N2cΔG) Strain Enhances Retrograde Synaptic Transfer and Neuronal Viability. Neuron *89*, 711–724. https://doi.org/10.1016/j.neuron.2016.01.004.

73. Wall, N.R., Wickersham, I.R., Cetin, A., De La Parra, M., and Callaway, E.M. (2010). Monosynaptic circuit tracing in vivo through Cre-dependent targeting and complementation of modified rabies virus. Proc. Natl. Acad. Sci. USA *107*, 21848–21853. https://doi.org/10.1073/pnas.1011756107.

74. Ciabatti, E., González-Rueda, A., Mariotti, L., Morgese, F., and Tripodi, M. (2017). Life-Long Genetic and Functional Access to Neural Circuits Using Self-Inactivating Rabies Virus. Cell *170*, 382–392.e14. https://doi.org/10.1016/j.cell.2017.06.014.

75. Jacobs, B.L., and Azmitia, E.C. (1992). Structure and function of the brain serotonin system. Physiol. Rev. *72*, 165–229. https://doi.org/10.1152/physrev.1992.72.1.165.

76. Vertes, R.P., and Linley, S.B. (2008). Efferent and afferent connections of the dorsal and median raphe nuclei in the rat. In Serotonin and Sleep: Molecular, Functional and Clinical Aspects, J.M. Monti, S.R. Pandi-Perumal, B.L. Jacobs, and D.J. Nutt, eds. (Birkhäuser Verlag), pp. 69–102. https://doi.org/10.1007/978-3-7643-8561-3_3.

77. Nectow, A.R., and Nestler, E.J. (2020). Viral tools for neuroscience. Nat. Rev. Neurosci. *21*, 669–681. https://doi.org/10.1038/s41583-020-00382-z.

78. Leng, G. (2018). The Heart of the Brain: the Hypothalamus and Its Hormones (The MIT Press) https://doi.org/10.7551/mitpress/11060.001.0001.

79. Thornquist, S.C., Pitsch, M.J., Auth, C.S., and Crickmore, M.A. (2021). Biochemical evidence accumulates across neurons to drive a network-level eruption. Mol. Cell *81*, 675–690.e8. https://doi.org/10.1016/j.molcel.2020.12.029.

80. Thornquist, S.C., Langer, K., Zhang, S.X., Rogulja, D., and Crickmore, M.A. (2020). CaMKII Measures the Passage of Time to Coordinate Behavior and Motivational State. Neuron *105*, 334–345.e9. https://doi.org/10.1016/j.neuron.2019.10.018.

81. Randi, F., Sharma, A.K., Dvali, S., and Leifer, A.M. (2023). Neural signal propagation atlas of Caenorhabditis elegans. Nature *623*, 406–414. https://doi.org/10.1038/s41586-023-06683-4.

82. Chen, Y., Lin, Y.C., Zimmerman, C.A., Essner, R.A., and Knight, Z.A. (2016). Hunger neurons drive feeding through a sustained, positive reinforcement signal. eLife *5*, e18640. https://doi.org/10.7554/eLife.18640.

83. Zhang, S.X., Kim, A., Madara, J.C., Zhu, P.K., Christenson, L.F., Lutas, A., Kalugin, P.N., Sunkavalli, P.S., Jin, Y., Pal, A., et al. (2025). Stochastic neuropeptide signals compete to calibrate the rate of satiation. Nature *637*, 137–144. https://doi.org/10.1038/s41586-024-08164-8.

84. Söderberg, J.A.E., Carlsson, M.A., and Nässel, D.R. (2012). Insulin-Producing Cells in the Drosophila Brain also Express Satiety-Inducing Cholecystokinin-Like Peptide, Drosulfakinin. Front. Endocrinol. (Lausanne) *3*, 109. https://doi.org/10.3389/fendo.2012.00109.

85. Yao, Z., and Scott, K. (2022). Serotonergic neurons translate taste detection into internal nutrient regulation. Neuron *110*, 1036–1050.e7. https://doi.org/10.1016/j.neuron.2021.12.028.

86. Wolf, F.A., Angerer, P., and Theis, F.J. (2018). SCANPY: large-scale single-cell gene expression data analysis. Genome Biol. *19*, 15. https://doi.org/10.1186/s13059-017-1382-0.

87. Choi, H.M.T., Beck, V.A., and Pierce, N.A. (2014). Next-generation in situ hybridization chain reaction: higher gain, lower cost, greater durability. ACS Nano *8*, 4284–4294. https://doi.org/10.1021/nn405717p.

88. Wang, W.X., and Lefebvre, J.L. (2022). Morphological pseudotime ordering and fate mapping reveal diversification of cerebellar inhibitory interneurons. Nat. Commun. *13*, 3433. https://doi.org/10.1038/s41467-022-30977-2.

89. Heiman, M., Kulicke, R., Fenster, R.J., Greengard, P., and Heintz, N. (2014). Cell type-specific mRNA purification by translating ribosome affinity purification (TRAP). Nat. Protoc. *9*, 1282–1291. https://doi.org/10.1038/nprot.2014.085.

90. Heiman, M., Schaefer, A., Gong, S., Peterson, J.D., Day, M., Ramsey, K.E., Suárez-Fariñas, M., Schwarz, C., Stephan, D.A., Surmeier, D.J., et al. (2008). A translational profiling approach for the molecular characterization of CNS cell types. Cell *135*, 738–748. https://doi.org/10.1016/j.cell.2008.10.028.

91. de Araujo Salgado, I., Li, C., Burnett, C.J., Rodriguez Gonzalez, S., Becker, J.J., Horvath, A., Earnest, T., Kravitz, A.V., and Krashes, M.J. (2023). Toggling between food-seeking and self-preservation behaviors via hypothalamic response networks. Neuron *111*, 2899–2917.e6. https://doi.org/10.1016/j.neuron.2023.06.006.

92. de Jong, J.W., Afjei, S.A., Pollak Dorocic, I., Peck, J.R., Liu, C., Kim, C.K., Tian, L., Deisseroth, K., and Lammel, S. (2019). A Neural Circuit Mechanism for Encoding Aversive Stimuli in the Mesolimbic Dopamine System. Neuron *101*, 133–151.e7. https://doi.org/10.1016/j.neuron.2018.11.005.

93. Lunde, A., and Glover, J.C. (2020). A versatile toolbox for semi-automatic cell-by-cell object-based colocalization analysis. Sci. Rep. *10*, 19027. https://doi.org/10.1038/s41598-020-75835-7.

STAR★METHODS

KEY RESOURCES TABLE

REAGENT or RESOURCE	SOURCE	IDENTIFIER
Antibodies		
Chicken polyclonal anti-GFP	Abcam	Cat# ab13970; RRID: AB_300798
Rabbit monoclonal anti-cFos	Cell Signaling Technology	Cat# 2250, RRID: RRID:AB_2247211
Rat monoclonal anti-mCherry	Thermo Fisher Scientific	Cat# M11217, RRID:AB_2536611
Rabbit polyclonal anti-DsRed	Takara Bio	Cat# 632496, RRID:AB_10013483
Goat Polyclonal TurboRFP	MyBioSource	Cat#: MBS448252
Mouse monoclonal anti-GFP (Heintz Lab TRAP anti-GFP 19F7)	MSKCC Antibody & Bioresource Core Facility	Cat# Htz-GFP-19F7, RRID:AB_2716736
Mouse monoclonal anti-GFP (Heintz Lab TRAP anti-GFP 19C8)	MSKCC Antibody & Bioresource Core Facility	Cat# Htz-GFP-19C8, RRID:AB_2716737
Bacterial and virus strains		
AAV5-IV-EGFPL10a	PNI viral core	N/A
AAV5-EF1a-double floxed-hChR2(H134R)-EYFP-WPRE-HGHpA	Addgene	Addgene AAV5; 20298-AAV5
AAV5-CAG-Flex-GCaMP6s-WPRE-SV40	Addgene	Addgene AAV5; 100842-AAV5
AAV1-hSyn-FLEx-mGFP-2A-Synaptophysin-mRuby	Addgene	Addgene AAV1; 71760-AAV1
AAV5-CMV-FLEX-TVAmCherry-2A-oG	PNI viral core	N/A
AAV5-hSyn-FLEx-Kir2.1-2A-GFP	PNI viral core	N/A
AAV5-hSyn1-SIO-stGtACR2-FusionRed	PNI viral core	N/A
Rabies Virus: CVS-N2c-dG-GFP/EnvA	Jefferson vector core	N/A
Chemicals, peptides, and recombinant proteins		
DHPC: 1,2-diheptanoylsn-glycero-3-phosphocholine	Avanti Polar Lipids	Cat# 850306
BSA: Bovine Serum Albumin	Jackson ImmunoResearch Labs	Cat# 001-000-162, RRID: AB_2336946
RNasin® Ribonuclease Inhibitor	Promega	Cat# N2515
SUPERaseIn™ RNase Inhibitor	Thermo Fisher Scientific	Cat# AM2696
Pierce™ Recombinant Protein L, Biotinylated	Thermo Fisher Scientific	Cat# 29997
Dynabeads™ MyOne™ Streptavidin T1	Thermo Fisher Scientific	Cat# 65602
PBS: Phosphate-Buffered Saline	Thermo Fisher Scientific	Cat# AM9625
HEPES	Thermo Fisher Scientific	Cat# J16924.K2
HBSS	Thermo Fisher Scientific	Cat# 14065056
$MgCl_2$	Thermo Fisher Scientific	Cat# AM9530G
KCl	Thermo Fisher Scientific	Cat# AM9640G
CCK: Cholecystokinin Octapeptide (sulfated)	Bachem	Cat# 4033010; CAS: 25126-32-3
Ex-4: Exendin-4	Tocris	Cat# 1933; CAS: 141758-74-9
PYY: Peptide YY (3-36)	Bachem	Cat# 4044052; CAS: 126339-09-1
5-HT: Serotonin hydrochloride	Millipore Sigma	Cat# H9523; CAS: 153-98-0
Amylin	Bachem	Cat# 4030201; CAS: 124447-81-0
Oxytocin	Tocris	Cat# 1910; CAS: 50-56-6
Methyl Cellulose	Fujifilm Wako	Cat# 133-17815; CAS: 9004-67-5
Ghrelin	Tocris	Cat# 1465; CAS: 258338-12-4
Saline	Ricca	Cat# 7210-16; CAS: 7647-14-5
Deposited data		
vTRAP RNA-seq data	This paper	GEO: GSE252409
STARmap/RIBOmap RNA-seq data	This paper	Zenodo: 10.5281/zenodo.14447775

(*Continued on next page*)

Continued

REAGENT or RESOURCE	SOURCE	IDENTIFIER
Experimental models: Organisms/strains		
Mouse: CCK-IRES-Cre: Ccktm1.1(cre)Zjh/J	The Jackson Laboratory	012706; RRID: IMSR_JAX:012706
Mouse: Rosa26-LSL-EGFPL10a: B6.129S4-Gt(ROSA)$^{26Sortm1(CAG-EGFP/Rpl10a,-birA)Wtp}$/J	The Jackson Laboratory	022367; RRID: IMSR_JAX:022367
Mouse: C57BL/6J	The Jackson Laboratory	000664; RRID: IMSR_JAX:000664
Software and algorithms		
GraphPad Prism 10.0	GraphPad Software	RRID:SCR_002798
MATLAB version R2023b	MathWorks	RRID:SCR_001622
R version 4.3.1	R Project for Statistical Computing	RRID:SCR_001905
Python version 3.10	Python Programming Language	RRID:SCR_008394
Fiji	http://fiji.sc	RRID:SCR_002285
Other		
Absolutely Total RNA Purification Kits	Agilent	400753

EXPERIMENTAL MODEL AND STUDY PARTICIPANT DETAILS

Mice

All experiments were approved by Columbia University's and Broad Institute of MIT and Harvard's Institutional Animal Care and Use Committee and were in accordance with National Institutes of Health guidelines. Both male and female mice were used for all studies. All mice were at least 6 weeks old at the time of surgery. Mice were housed at a constant temperature of ~22.5°C, with humidity of ~45%, and a 12 hr light-dark cycle (with light on at 7am). Mice were initially group housed, followed by single housing prior to experiments, unless otherwise stated. Mice were given *ad libitum* access to chow (PicoLab Rodent Diet 5053) and water, unless otherwise stated. All mice used in these studies are on a C57BL/6J background. Sources and genotypes of mice can be found in the key resources table.

METHOD DETAILS

STARmap/RIBOmap protocol

Eight week old, male C57BL/6 mice were used for STARmap and RIBOmap sequencing. Mice were anesthetized under isoflurane and transcardially perfused with 1x PBS (Gibco). Brains were collected, placed in OCT (Fisher), and frozen in 2-methyl-2-butanol (Sigma) on dry ice.

Sample preparation

12-well glass bottom plates (MatTek) were plasma treated (100W, 2% O_2) for 45 seconds. Immediately following plasma activation, plates were treated with 1% methacryloxypropyltrimethoxysilane (Bind-Silane, GE Healthcare) for 1 hour, as previously described.[40] Plates were washed at least 3 times with 95% ethanol and allowed to dry. Plates were then coated in 0.1mg/mL poly-D-lysine (PDL, Sigma) overnight. Plates were washed extensively with RNase-free water and allowed to dry before use.

Coronal brain slices from DRN were collected at 20μm on a cryostat (Leica CM1950) into pretreated plates. Tissue sections were fixed with 4% PFA (Electron Microscopy Sciences) in 1x PBS for 10 minutes at room temperature (RT) and permeabilized with pre-chilled 100% methanol (Sigma) overnight at -20°C. Samples were allowed to dry completely before rehydrating with PBSTR (1x PBS with 0.1U/μL SUPERase-IN; ThermoFisher) containing 1% yeast tRNA (ThermoFisher) and 100mM Glycine (VWR) at RT for 15 minutes.

Library construction

SNAIL probes were purchased from IDT as oPools (separate oPools were purchased for STARmap padlock probes, RIBOmap padlock probes, and shared primer probes; see Table S1 for sequence information. Stock SNAIL probes were dissolved to 50nM per probe in water. Brain slices were incubated in 300μL of hybridization buffer (2x SSC (Sigma-Aldrich), 10% formamide (Calbiochem), 1% Tween-20, 20 mM ribonucleoside vanadyl complex (New England Biolabs), 0.1 mg/mL yeast tRNA, 0.1 U/μL SUPERaseIn) at 40°C for 36 hours with gentle shaking. STARmap sections were incubated with 5nM STARmap padlock probes and 5nM primer probes. RIBOmap sections were incubated with 5nM RIBOmap padlock probes, 5nM primer probes, and 100nM splint probes.

Samples were then washed at 37°C for 20 minutes with 600μL PBSTR twice, followed by one wash with high salt buffer (PBSTR in 4x SSC). After a brief rinse with PBSTR at RT, samples were incubated in ligation mixture (0.25 U/μL T4 DNA ligase (Thermo Scientific), 1x T4 ligase buffer, 0.2 mg/mL BSA (New England Biolabs), 0.2 U/μL SUPERase-In) for 2 hours at RT with gentle shaking.

Samples were washed 2x with 600μL PBSTR, before incubating with 300μL rolling-circle amplification mixture (0.5 U/μL Phi29 DNA polymerase (Thermo Scientific), 1x Phi29 reaction buffer, 250 μM dNTP mixture (New England Biolabs), 0.2 mg/mL BSA, 0.2 U/μL SUPERase-In and 20 μM 5-(3-aminoallyl)-dUTP; Invitrogen) at 4°C for 30 minutes to equilibrate the samples, followed by 30°C for 2 hours for amplification.

The samples were next washed twice in 600 μL PBST (1x PBS, 0.1% Tween-20) and treated with 400μL 20mM acrylic acid NHS ester (Sigma) in 1x PBS overnight. Samples were washed briefly with 600μL PBST once, then incubated with 400μL monomer buffer (4% acrylamide; Bio-Rad), 0.2% bis-acrylamide (Bio-Rad), in 2x SSC) for 30 min at RT. After removing the monomer buffer, 25 μL of polymerization buffer (0.2% ammonium persulfate (Sigma-Aldrich), 0.2% tetramethylethylenediamine (Sigma-Aldrich) in monomer buffer) was added to the center of the sample and was immediately covered with a Gel Slick 12 mm coverslip and incubated for 1 hour at RT under nitrogen gas. Following gelation, the tissue-gel hybrids were washed with PBST briefly, and digested with Proteinase K buffer (0.2 mg/mL proteinase K; Invitrogen) in 50 mM Tris-HCl 8.0, 100 mM NaCl, 1% SDS (Calbiochem) at RT for 1 hour. Samples were then washed with 600μL of PBST at RT three times for 5 minutes each and stored at 4°C until sequencing.

In situ sequencing

Before SEDAL sequencing, samples were washed twice with stripping buffer (60% formamide and 0.1% Triton X-100 in water) and treated with dephosphorylation buffer (0.25 U/μL Antarctic Phosphatase (New England Biolabs), 1x reaction buffer, 0.2 mg/mL BSA) at 37°C for 1 hour. Each cycle of SEDAL sequencing began with two washes with stripping buffer (10 minutes each) and three washes with PBST (5 minutes each). Sample was incubated with sequencing by ligation mixture (0.2 U/uL T4 DNA ligase, 1× T4 DNA ligase buffer, 0.2 mg/mL BSA, 10 μM reading probe, and 300 nM of each of the 16 two-base encoding fluorescent probes) at RT overnight. After three 10 min washes with wash and imaging buffer (10% formamide in 2x SSC) and DAPI staining (Invitrogen) following manufacturer's instructions, the samples were imaged in wash and imaging buffer.

Imaging was performed on a Leica SP8 scanning confocal microscope with a white light laser and using a 40X oil immersion objective (NA = 1.30). Z-stacks were collected with a 0.35μm step size to conform to Nyquist requirements, with a voxel size of 194nm x 194nm. DAPI was acquired during the first imaging round to enable image registration. In total, 4 STARmap and 4 RIBOmap (adjacent sections to STARmap) were acquired.

STARmap and RIBOmap Data Analysis

After imaging, data were processed and analyzed as per below.

Image pre-processing

Image deconvolution was performed using Huygens Essential (Scientific Volume Imaging), using the classic maximum likelihood estimation method, with a signal-to-noise ratio of 10, for 10 iterations. Image registration, spot calling, and barcode decoding were performed following previous reports.[40,44]

Cell segmentation

A maximum intensity projection of the stitched DAPI channel was generated, with a median filter applied to remove high-frequency noise. Nuclei were automatically identified by applying a pretrained 2D machine learning model (Versatile model) from the StarDist 2D plugin in Fiji, with the following parameters: percentile low: 1, percentile high: 99, probability: 0.65, overlap threshold: 0.40. A composite, maximum projected image combining all amplicon imaging channels was thereafter created to represent the cell boundary. A Gaussian filter with sigma of 5 was applied to the amplicon image, and was binarized with the Otsu thresholding strategy. To better incorporate the amplicons around the peripheral regions of the cell bodies, a binary dilation with disk structure element (r = 10) was applied on the mask. Finally, a marker-based watershed transform was performed to segment the binary mask representing cell bodies. Points overlapping each segmented cell region in 2D were then assigned to that cell to compute a per-cell gene expression matrix.

Quality control for cells

We excluded low-quality cells following standard data preprocessing procedures in Scanpy.[86] Each STARmap and RIBOmap sample was first processed separately to remove low-quality cells. We set the minimum gene number per cell to 5 and the minimum cell number per gene to 10. We additionally used the median absolute deviation (MAD) method to estimate the threshold for reads per cell filtering as shown by the following equation:

$$\text{Lower boundary} = \text{median}(\text{reads per cell}) - 3 \times \text{MAD}$$

$$\text{Upper boundary} = \text{median}(\text{reads per cell}) + 3 \times \text{MAD}$$

After filtering, we obtained a cell-by-gene matrix containing expression information for 85,072 cells (across 8.7 million RNA reads). The data was then normalized according to the median of the number of transcripts per cell, logarithmically transformed, and scaled.

RIBOmap and STARmap samples were combined following pre-processing, followed by batch correction using the combat function. Harmony integration[43] was performed to the combined dataset to create a joint PCA embedding as previously described.[40]

Cell type annotations for full dataset

We followed previously described methods and code for cell-type annotations and clustering.[44] We first used Harmony to integrate the STAR/RIBOmap dataset with a published scRNA-Seq dataset of the mouse DRN,[45] consisting of 39,411 cells, of which 2,041 cells belong to the neuronal lineage. Although this dataset contained a low number of neurons, we found it to be a useful reference for annotating non-neuronal populations in our dataset due to the low number of non-neuronal cell-type markers in our experiments.

We used the overlapping 227 genes between STAR/RIBOmap and scRNA-Seq datasets to compute the adjusted principal components (n_comps = 20) and neighborhood graph of observations (n_neighbors = 70). Leiden clustering of STAR/RIBOmap cells was performed with a resolution of 2. Annotations of main-level STAR/RIBOmap cell clusters were determined by projecting scRNA-Seq cell-type labels onto the joint manifold. We transferred labels from scRNA-Seq to the STAR/RIBOmap clusters based on the following: within each cluster, we checked the cell-type labels of scRNA-seq cells. If the number of top-1 scRNA-Seq cell-type label within the joint cluster exceeded 85% for neurons, or 50% for non-neurons, it indicated successful integration for the cluster. We therefore assigned this dominant top-1 scRNA-Seq cell-type label to the STAR/RIBOmap cluster. Otherwise, we regarded the integration as unsuccessful and temporarily labeled the cluster as ''NA''.

We then investigated the spatial cell distributions and cluster-specific expression patterns for each cluster to confirm the cell-type assignments of successfully integrated clusters, and to manually annotate ''NA'' clusters. Cell clusters that did not reside within the DRN, which consisted of the majority of ''NA'' clusters were annotated as ''Non-DRN Cell Types''. Clusters that contained low cell numbers and which did not present notable patterns in spatial distribution nor gene expression were labeled as ''NA''. Finally, we merged clusters representing the ''GABAergic'' and ''Glutamatergic'' lineages for the full dataset analysis.

To further improve the cell-type classifications, we calculated the Euclidean distance from each cell to the centroid of the cluster it belongs to on the UMAP embedding. Based on the distribution of the Euclidean distances for each cluster, a distance threshold was manually determined, and cells with a distance value greater than the threshold were labelled as ''NA'', and excluded from downstream analyses.

Cell type annotations for DRN neurons

From the full STAR/RIBOmap dataset, we first subsetted out cells that belong to the neuronal lineage, and for which at least a subset were enriched within the DRN. Together, we identified 33,591 DRN neurons for downstream analyses, comprising the ''TH'', ''Serotonergic'', ''GABAergic'', Glutamatergic'', ''GABAergic/Glutamatergic'', and ''Glu3 (vlPAG excitatory)'' cell clusters. We note that the ''Non-DRN Peptidergic'' neurons were excluded from further analyses as they were not enriched within the DRN. Additionally, this cluster of cells was annotated to be ''Peptidergic'' based on assignment from scRNA-Seq, although the published dataset only captured peptidergic neurons from the EW, not the DRN.[45] We additionally subsetted cells that belong to the neuronal lineage from scRNA-Seq, consisting of 2,041 cells.[45]

We followed the methods described above for annotation of neuronal clusters, with a few modifications. We used Harmony to integrate the subsetted STAR/RIBOmap neuronal dataset with the published scRNA-Seq neuronal dataset. We used the overlapping 227 genes between STAR/RIBOmap and scRNA-Seq to compute the adjusted principal components (n_comps = 11) and neighborhood graph of observations (n_neighbors = 50). Leiden clustering of STAR/RIBOmap cells was performed with a resolution of 0.6. We first visualized the projection of scRNA-Seq cell-type labels onto the joint manifold. We transferred labels from scRNA-Seq to STAR/RIBOmap cells if the number of top-1 scRNA-Seq cell-type label within the joint cluster exceeded 85%. This consisted of the ''TH'', ''GABAergic 1'', ''GABAergic 2'', ''Serotonergic'', ''Glutamatergic 1'', and ''GABAergic/Glutamatergic'' clusters. We additionally confirmed the transferred labels, and annotated the remaining clusters based on cell-type spatial distributions and cluster-specific expression patterns. Lastly, we calculated the Euclidean distance from each cell to the centroid of the cluster it belongs to in the UMAP embedding. Cells with Euclidean distances greater than a manually selected threshold were excluded from further analyses.

Subclustering analysis of TH neurons

From the STAR/RIBOmap neuronal dataset, we first subsetted out cells which belong to the TH cluster, consisting of 980 cells. We performed Leiden clustering with a resolution of 0.5 to identify three TH subclusters.

Single molecule fluorescence *in situ* hybridization (smFISH)

HCR amplification-based smFISH was performed following previous protocols.[87,88] HCR 3.0 probes were purchased from Molecular Instruments. All steps were performed under RNAse-free conditions and using molecular grade, RNAse-free water (Life Technologies). 12 well, glass-bottom plates were treated with Bind-Silane and PDL, following procedures described in the STARmap section above. Animals for smFISH were perfused with PBS, followed by 4% PFA. Brains were post-fixed in 4% PFA for 3 hours at RT and were cryopreserved in 30% sucrose until they sank (~24 hours). Coronal sections of the DRN were obtained at 30μM onto glass-bottom plates. Prior to smFISH, samples were permeabilized in 70% ethanol overnight at 4°C. Coverslips were allowed to dry completely before hybridization. Primary probe hybridization was performed at 2μM probe concentration in HCR hybridization buffer (Molecular Instruments) at 37°C overnight. Samples were additionally hybridized with a 1μM poly(dT) clearing probe. 3x washes were performed

in wash buffer (Molecular Instruments) at 40°C, which was followed by 3x washes in 5x SSCT (0.1% triton-X) at RT. Sample gelation was performed following protocols from the STARmap sections above. Clearing buffer was prepared by mixing 1:100 proteinase K, 50mM Tris-HCl pH 8, 1mM EDTA, 0.5% Triton-X, 500nM NaCl, and 1% SDS. Samples were allowed to clear overnight at 37°C. After clearing, samples were washed 3x in 5x SSCT prior to HCR amplification. HCR hairpins were prepared by heating to 95°C for 90 seconds and allowed to cool to room temperature slowly over 30 minutes. Amplification solutions were prepared by mixing 10μL H1 and 10μL H2 in 500μL amplification buffer for each well. Amplification occurred in the amplification buffer (Molecular Instruments) overnight at RT. Following amplification, samples were washed 3x in 5x SSCT, stained with 1:3000 DAPI (Thermofisher) for 10 minutes at RT, and mounted in Fluoromount-G mounting media.

Molecular profiling using vTRAP

AAV5-IV-GFPL10 was stereotactically injected into the DRN of CCK-IRES-Cre mice. Immunoprecipitations (IPs) were then performed at least 4 weeks later, allowing for GFPL10 expression and ribosomal integration. Two biological replicates were used, each consisting of tissues pooled from 5 mice (3 males and 2 females). Affinity purification of EGFP-tagged polysome was performed as described elsewhere.[51,89] Briefly, streptavidin-conjugated magnetic beads were prepared in an RNase-free environment by first binding them with Biotinylated protein L and then with anti-EGFP monoclonal antibodies, 19C8 and 19F7.[90] Brains were then extracted, after which DRN-containing tissue was collected under a dissection scope (Stemi 305, Zeiss). Tissue was then homogenized using a clean glass homogenizer on ice. The clarified supernatant of the tissue homogenates was allowed to incubate overnight with the anti-EGFP magnetic beads to immunoprecipitate translating polysomes. RNA was then extracted using the Absolutely RNA Nanoprep kit (Agilent), after which RNA was analyzed for quality and quantity using a Bioanalyzer (Pico Chip). All RNA RIN values were > 9. High-throughput RNA-seq was then performed using the following protocol. First, cDNA synthesis was performed with the Clontech SMART-seq Ultra Low v4 kit (Takara), followed by library preparation using Nextera XT (Illumina). Libraries were then sequenced using a NovaSeq 6000 (Illumina). Samples were multiplexed in each lane, and paired-end 100bp reads were performed for each sample. Base calling was performed using RTA (Illumina), and bcl2fastq2 (version 2.19) was used for file conversion from BCL to fastq (this was coupled with adaptor trimming). Pseudoalignment was performed using Kallisto (0.44.0) with the reference Ensembl v96 (GRCm38.p6). Differential gene expression between IP and Input was determined using DESeq2. Gene ontology analysis was performed on the top 100 most highly enriched genes at a significance value of padj < 0.01 using ShinyGO 0.77. An FDR cutoff of 0.05 was used with a minimum pathway size of 2 genes. Results were plotted using custom code in R.

Intracranial viral injections and fiber optic implantations

Animals were anesthetized using 2-3% isoflurane and mounted onto a stereotaxic surgical frame (David Kopf). A small craniotomy was performed using an automated drill (Osada Inc) at the measured coordinates. Viral vectors were injected locally into the brain using Nanoject III (Drummond Scientific, PA) with a pulled glass pipette at a rate of 50 nl of virus per min. AAVs carrying Cre-dependent GFPL10 (600 nl/animal), TVA-mCherry-2A-oG (300 nl), and GCaMP6s (600 nl) were injected straight into the DRN at a coordinate of 4.5 mm posterior, 0 mm lateral, -3.0 mm deep measured with respect of bregma. AAVs carrying Cre-dependent ChR2 (300 nl), ACR2 (500 nl), Kir2.1 (700 nl), EYFP (volume matched to treatment) and G-deleted rabies (600 nl) were injected into the DRN at a 16° angle (4.5 mm posterior, 0.8 mm lateral, -3.1 mm deep from bregma). All viral injection volumes were determined based on transduction in pilot studies. For all optogenetic experiments, fiber optic cannulae with a flat fiber tip, 200 μm core diameter, and numerical aperture of 0.22 were used (Doric Lenses Inc). Following viral injections and retraction of the Nanoject III glass pipette, optic cannulas were inserted using cannula holders into the same coordinate as used for the viral injection but at a Z position 500 μm above the viral injection site. For *in vivo* fiber photometry recordings, fiber optic cannulae with a flat fiber tip, 400 μm core diameter, and numerical aperture of 0.48 were used. After injecting GCamP6s carrying AAV, optic cannulas were implanted in the exact same coordinates as the virus. Optical fiber ferrules were fixed with quick adhesive cement (C&B Metabond, Parkell) after all implantations.

Gastric catheter implantation surgeries

GCaMP6s-expressing CCK-IRES-Cre mice with optic cannula implanted over the DRN were used for gastric catheter implantation surgeries. At least 4 weeks were allowed to elapse between two surgeries for full animal recovery. Animals were starved for ~6 hours prior to surgery and were allowed to refeed on a regular diet for about an hour for stomach distension to aid in visualization during surgery. Midline abdominal skin and underlying muscle layer incisions were made from the xiphoid cartilage to the mid-abdomen to expose the stomach in isoflurane-anesthetized animals placed on a heating pad. A gastric catheter (Instech), assembled by placing surgical mesh (eSutures) was sutured at the fundus with around 3 mm of the catheter inserted inside the stomach. The other end of the catheter was pulled through a subcutaneous tunnel, which exited through an incision made along the dorsal neck and was attached to a vascular button (VAB62BS/22, Instech) positioned at the dorsal end of the catheter. After suturing, approximately 0.1 ml of saline was gently infused into the stomach using the saline-filled sterile syringe attached to the proximal end of the catheter to ensure no leakage.

Fos labeling

CCK-IRES-Cre mice crossed to reporter (EGFPL10a) mice were singly housed for at least 5 days before experiments and were randomized into one of three groups: starved, refed, or fed *ad libitum*. Animals from both starved and refed groups were food-deprived

for 16 hours, with the refed group allowed to have access to food for 2 hours prior to perfusion. Animals from the fed group were allowed to have free access to food and were perfused the same day as mice from the starved and refed groups.

Optogenetic stimulation

For all optogenetic studies, a blue light DPSS Laser of 473nm wavelength (Laserglow) was used to deliver light pulses through optic cannulae. For optical activation studies, light power of 10-12 mW, measured at the tip of the optic cannula, with a pulse width of 10 ms was used. Different frequencies were generated using an open-source pulse train generator (Pulse Pal, Open Ephys). For optical inhibition studies, we used continuous light stimulation with a power of 5-6 mW measured at the tip of the optic cannula. Animals were tethered to a patch cord connected to a fiber optic rotary joint for habituation for at least 15 min prior to all optogenetic behavioral studies.

Behavioral studies

Animals of both sexes were used in all behavioral studies and effort was made to match for littermates among control and experimental groups whenever possible. Animals were singly housed for at least one week prior to starting behavioral studies.

Feeding and drinking assays

Food intake studies were done in food-deprived animals by periodically measuring food pellet(s) dropped on the metal grid of the home cage. For all overnight starvation studies, animals were food deprived starting around the onset of the dark cycle for 16 hours with water access. For water deprivation studies, animals were water deprived for 24 hours with *ad libitum* access to food. For the pre-stimulation studies, food-deprived animals received a 10 Hz blue light pulse for a defined time period (0, 15, 30, or 60 min) before being given access to food. Drinking assays were performed in water-deprived mice, where total water intake was measured in a 30 min time window.

Meal pattern analysis using FED3 devices

The pellet-dispensing device FED3,[62] sourced through Open Ephys, was used for meal pattern analysis. Animals were habituated with a free feeding program using a home cage FED3 device, where pellets were delivered 5 s after retrieval of the prior pellet for at least 3 days, with regular chow available. Animals were then habituated with a free feeding program of FED3 with no regular chow. The FED3 was subsequently removed from home cage at the time starvation onset and was replaced during the timing of experimentation. A meal was defined as a sliding 60-second window for pellet retrieval (i.e., a meal's end is defined as having had 60 seconds elapse without a subsequent pellet retrieval).[62,91]

Closed-loop optogenetic experiments

For closed-loop optogenetic activation experiments, food-deprived animals were given access to food pellets through the FED3 device. Five seconds after retrieving each pellet, animals were given a brief blue light pulse at 10 Hz for five seconds. The laser was triggered directly through the FED3 device connected using a BNC adapter.

Open field test (OFT)

Individual mice were placed in a cubic open field chamber of 43 x 43 x 43 cm during the experiment. The chamber comprises four plastic walls and a detachable floor of the same material. Animals were allowed to move freely throughout the arena for 15 min. 10 Hz blue light stimulation was applied during the middle 5 min epoch to activate CCK neurons optogenetically, a process aimed at studying the neural basis of anxiety-related behavior. Animal behavior was continuously recorded using a video camera positioned above the arena. The camera was controlled by EthoVision XT (Noldus, Netherlands), and movement in different epochs was calculated. The arena was divided into a center (28 x 28 cm) and a periphery region to calculate anxiety-related behavior. The arena was carefully cleaned with 3% hydrogen peroxide between each trial.

Real-time place preference (RTPP)

Each experimental mouse was placed in a two-compartment (60 x 30 cm) chamber consisting of white plastic walls and floors. Within the chamber were two equal-sized compartments separated by removable slider openings (10 x 30 cm each) in which the mice could move freely between left and right compartments. They were allowed to move freely between compartments for 20 minutes, and entry into one of the two sides resulted in photostimulation (Stimulation side). The side paired with photostimulation was counterbalanced between animals. A video camera positioned directly above the arena tracks mouse movement (EthoVision XT, Noldus, Wageningen, Netherlands). A two-way ANOVA with a Sidak multiple comparisons test was used to test for significance.

Intragastric infusion (IGI) studies

All IGI studies were performed in starved animals. Animals were attached to photometry patch cords and infusion cannulae and habituated for at least 15 min prior to recordings. Infusion tubing was washed with MQ water and primed with the solution to be infused to avoid any dead volume. A total volume of 0.75 ml solution was delivered at a rate of 50 μl/min using a syringe infusion pump (AL-1000, World Precision Instruments). Methylcellulose solution at a concentration of 0.5% was chosen for its high viscosity

of 400 cP. Normal saline was chosen for its high osmolarity of ~308 mOsm/L. Water and methylcellulose have similarly low osmolarities.[67] Water and normal saline have similarly low viscosities. The Ensure solutions were provided at either 0.1 or 1 kcal per ml.

Fiber photometry recording and data analysis

A custom-built camera-based fiber photometry system was used for recordings of GCaMP6s-based calcium signals as a proxy for neuronal activity which is based on a simplified version of those used by Kim et al.[61] and was set up as described elsewhere.[92] Time stamps in the experiments were acquired using TTL pulses generated by the video tracking software (Ethovision), or by delivering an input pulse directly from the FED3 device using an audio to BNC adapter, or via a custom-built switch on an Arduino UNO R3 microcontroller board (with code written in Arduino script). Fluorescence signals were acquired using custom acquisition code written in MATLAB.[92] All recorded signals (dF/F) were normalized to z-score the signals.

To normalize the mealtime with z-scored signals during the first meal after food deprivation across animals, we first set up a series of standard time points from – 0.5 to 1.5 (where a meal is initiated at timepoint 0 and ends at 1), interpolated the data set to get the value of each meal at each standard time point, and calculated mean and SEM. For AUC calculations, a baseline was first set by averaging z-scored values across 20 seconds prior to the first retrieval. The area was then calculated from each sub-interval according to the trapezoidal rule, starting from the time of the first pellet retrieval of the meal until the last retrieval, plus 10 seconds. If a trapezoid was below the baseline, the area was set to 0. A linear regression model was then fitted to the data.

To study feeding microstructure while recording CCK activity through fiber photometry, animals that had undergone GCaMP6s surgery were fasted overnight. The animals were allowed to acclimate in a clean cage for more than 15 min before the trial. They were then given access to a single chow pellet in the cage for approximately 30 minutes. The entire session was recorded using a Basler CMOS camera at a frame rate of 25 fps and the videos were manually analyzed afterward.

Monosynaptic viral tracing using rabies virus

For monosynaptic retrograde tracing with G-deleted rabies virus (RV*d*G), Cre-dependent AAV was first injected into the DRN to drive the expression of the TVA receptor and optimized Rabies Glycoprotein (oG) (TVAmCherry-2A-oG).[74] Fourteen days later, the EnvA-pseudotyped N2C strain of rabies virus (dG-GFP/EnvA) was injected into the DRN.[72] Animals were sacrificed and examined for expression of fluorescent protein 10 days after the injection of rabies virus. For counting input cells, sections representative across the whole brain were mounted and imaged with an epifluorescence microscope (BZ-8000, Keyence). Each slice was matched to the corresponding coronal section of Paxinos' mouse brain atlas. Input cells were manually counted using a Fiji plugin to obtain the total number of input cells per brain area, counting the hemisphere with the highest number of input cells. The percentage of input cells was calculated from each of the brain regions, taken as the ratio of the total number of GFP-labeled cells in each brain (with the injection site excluded).

The following abbreviations are used in Figure 6: Acb, nucleus accumbens; Arc, arcuate nucleus; BLP, basolateral amygdala, posterior; BMA, basomedial amygdala; BNST, bed nucleus of the stria terminalis; CeA, central amygdala; Cg, cingulate cortex; Cpu, caudate putamen; DTT, dorsal tenia tecta; Gi, gigantocellular reticular nucleus; IC, inferior colliculus; InCo, Intercollicular nucleus; IO, inferior olive; IPAC, interstitial nucleus of the posterior limb of the anterior commissure; LC, locus coeruleus; LDTg, laterodorsal tegmental nucleus; LHA, lateral hypothalamus; LHb, lateral habenula; LPB, lateral parabrachial nucleus; LPO, lateral preoptic area; LS, lateral septum; M1, primary motor cortex; M2, secondary motor cortex; MD, mediodorsal thalamus; MeA, medial amygdala; MPB, medial parabrachial nucleus; MPO, median preoptic nucleus; MRN, midbrain reticular nucleus; NTS, nucleus of the solitary tract; OC, orbital cortex; PAG, periaqueductal gray; pLC, peri-locus coeruleus; PMN, premamillary nucleus; PCG, pontine central grey; PPTg, pedunculopontine tegmental nucleus; PRN, pontine reticular nucleus; PVH, paraventricular hypothalamus; RMg, raphe magnus; S1, primary somatosensory cortex; SC, superior colliculus; SNr, substantia nigra pars reticulata; SubC, subcoeruleus nucleus; VP, ventral pallidum; VTA, ventral tegmental area; ZI, zona incerta.

The following abbreviation are used in Figure S7: Ob, olfactory bulb; Septum, septal nuclei, anterior; NAc, nucleus accumbens, shell; ACC, cingulate nucleus, anterior; BNST, bed nucleus of the stria terminalis; OFC, orbitofrontal cortex; DTT, dorsal tenia tecta; aINS, insular cortex, anterior; PC, piriform cortex; M1, primary motor cortex; CeA, central amygdala; BLA, basolateral amygdala; BLP, basolateral amygdala, posterior; MnPOA, median preoptic area; MPOA, medial preoptic area; PVH, paraventricular hypothalamus; LHA, lateral hypothalamic area; Arc, arcuate nucleus; DMH, dorsomedial hypothalamus; VMH, ventromedial hypothalamus; PH, posterior hypothalamus; ZI, zona incerta; LHb, lateral habenula; PVT, paraventricular thalamus; Xi, xiphoid thalamic nucleus; VTA, ventral tegmental area; SN, substantia nigra; RLi, rostral linear nucleus; SuM, supramammillary nucleus; antPAG, periaqueductal gray, anterior; DRN, dorsal raphe nucleus; MnR, median raphe nucleus; Pn, pontine nuclei; postPAG, periaqueductal gray, posterior; PBN, parabrachial nuclei; pLC, peri-locus coeruleus; DTg, dorsal tegmental nucleus; antNTS, nucleus of the solitary tract, anterior; Rpa, raphe pallidus; Gi, gigantocelluar nucleus; postNTS, nucleus of the solitary tract, posterior; AP, area postrema.

Anterograde viral tracing

To identify the direct downstream projections of CCK neurons, an AAV expressing Cre-dependent soluble GFP and a synaptophysin-mRuby fusion protein was injected into the DRN of CCK-IRES-Cre mice. The AAV construct (AAV5-hSyn-GFP-2A-synaptophysin-mRuby) drives the expression of cytosolic GFP and presynaptic mRuby fluorescent protein. Animals were sacrificed and examined for fluorescent protein expression approximately six weeks after injection of the virus. Images were captured using an

epifluorescence microscope (BZ-8000, Keyence) under standardized settings, and image analysis was performed with Fiji. Regions of interest (ROIs) were defined by GFP expression, and measurements of the area and the mean pixel density for each ROI were recorded. Background pixel density was subtracted for each ROI, and signal intensities were averaged across mice to assess GFP and synaptophysin-mRuby expression levels in each brain region.

Whole-brain Fos mapping

EYFP- (control) and ChR2-expressing animals that underwent optogenetic activation for one hour were used for whole-brain Fos mapping. As with the above behavioral studies, optical activation was conducted with a light power of 10-12 mW (measured at the tip of the optic cannula) and a pulse width of 10 ms. One hour after cessation of stimulation (2 hr after laser stimulation onset), brains were extracted. After histological preparation and Fos staining, representative brain sections across the whole brain were mounted, imaged, and quantified. Images were captured using an epifluorescence microscope (BZ-8000, Keyence). Images were then matched to the corresponding section of the Paxinos' mouse brain atlas to identify activated brain regions. Fos-expressing cells were counted in Fiji, aided by the Colocalizer Cell Counter plugin.[93] The semi-automated counter was used to identify the 2D maxima, and the noise tolerance settings were kept consistent. Any background noise was removed, and counting was verified manually. All quantified brain areas were matched across all animals of the control and ChR2 groups. The fold-change of Fos expression in the ChR2-expressing animals was calculated over the average Fos expression in the control group.

Histology

Mice were euthanized with CO_2 inhalation and were quickly subjected to serial transcardial perfusion first using ~30 ml ice-cold phosphate-buffered saline (PBS) and then ~50 ml ice-cold 10% formalin solution (Fisher Scientific). After perfusion-fixation, brains were carefully removed, post-fixed in a 10% formalin solution at 4°C overnight on an end-to-end rotator, dehydrated by immersing in PBS containing 30% sucrose at 4°C until sinking to the bottom of the tube, and finally embedded in OCT compound for subsequent cryosectioning. Coronal sections of 40 μm thickness were made using a cryostat (Leica Microsystems), and slices were preserved in PBS containing 0.02% of NaN_3 at 4°C until stained. For staining, coronal brain sections were permeabilized (in 0.1% Triton X-100 in PBS, PBST), blocked (5% host-specific serum, 3% BSA, and 0.1% Triton-X-100 in PBS), and then incubated with primary antibodies at 4°C overnight. After washing, sections were then incubated with secondary antibodies for 1 hr at RT. For Fos staining, sections were permeabilized (in 0.1% PBST), blocked (in 10% Normal Goat Serum (NGS) in 0.3% PBST) for 1 hr at RT, incubated with primary antibodies at 4°C overnight, and secondary antibodies for 2 hr each at RT with streptavidin-based amplification. Slices were mounted, counterstained with DAPI in 50% glycerol solution, and examined with an epifluorescence microscope (BZ-8000, Keyence) and/or confocal microscope (LSM710, Zeiss).

QUANTIFICATION AND STATISTICAL ANALYSIS

Statistical analyses in all the figures were performed using GraphPad PRISM 10 or R. Mice were randomized into treated or control groups. All sample sizes (n), and what they represent, can be found in the figure legends. Data with error bars are presented as mean ± SEM, unless stated otherwise. Statistical tests used were the following: *t*-test or two-way ANOVA with *post hoc* testing, unless otherwise specified. For RNA-seq analyses using DESeq2, data are provided as average normalized counts for all samples (baseMean), fold-enrichment (log2FoldChange), standard error (lfcSE), and Wald statistic (stat), as well as the non-adjusted (Wald test) p-value (pvalue) and Benjamini-Hochberg adjusted p-values (padj). For GO analysis, the top 100 most highly enriched genes were selected, with a p-value cut-off of < 0.01 (enrichment FDR < 0.05). For all studies, significance was defined as $p < 0.05$. In the figures, asterisks denote statistical significance at the following levels: *$p < 0.05$, **$p < 0.01$, ***$p < 0.001$, ****$p < 0.0001$, $^{\dagger}p < 0.05$, $^{\dagger\dagger}p < 0.01$.

Supplemental figures

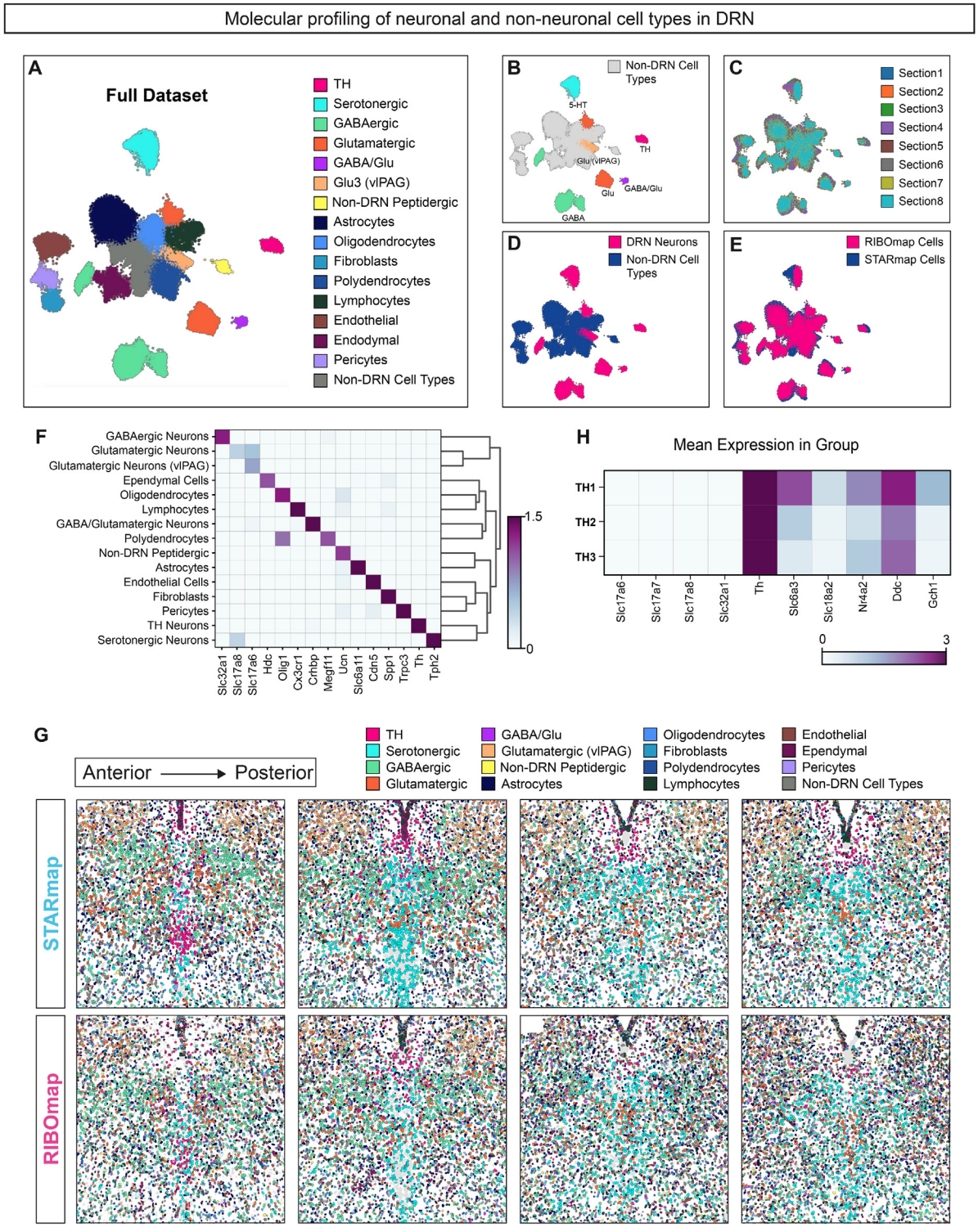

(legend on next page)

Figure S1. Characterization of DRN cell types using STARmap/RIBOmap, related to Figure 1

(A) UMAP for all DRN cell types.

(B–E) UMAP of sequenced cells organized by DRN neuronal labels (B), distribution across sections (C), anatomic distribution (D), and sequencing modality (E).

(F) Heatmap of expression levels for differentially expressed transcripts among cell clusters.

(G) Projection of cell clusters onto their anatomical positions.

(H) Heatmap of expression levels for differentially expressed transcripts among TH+ clusters.

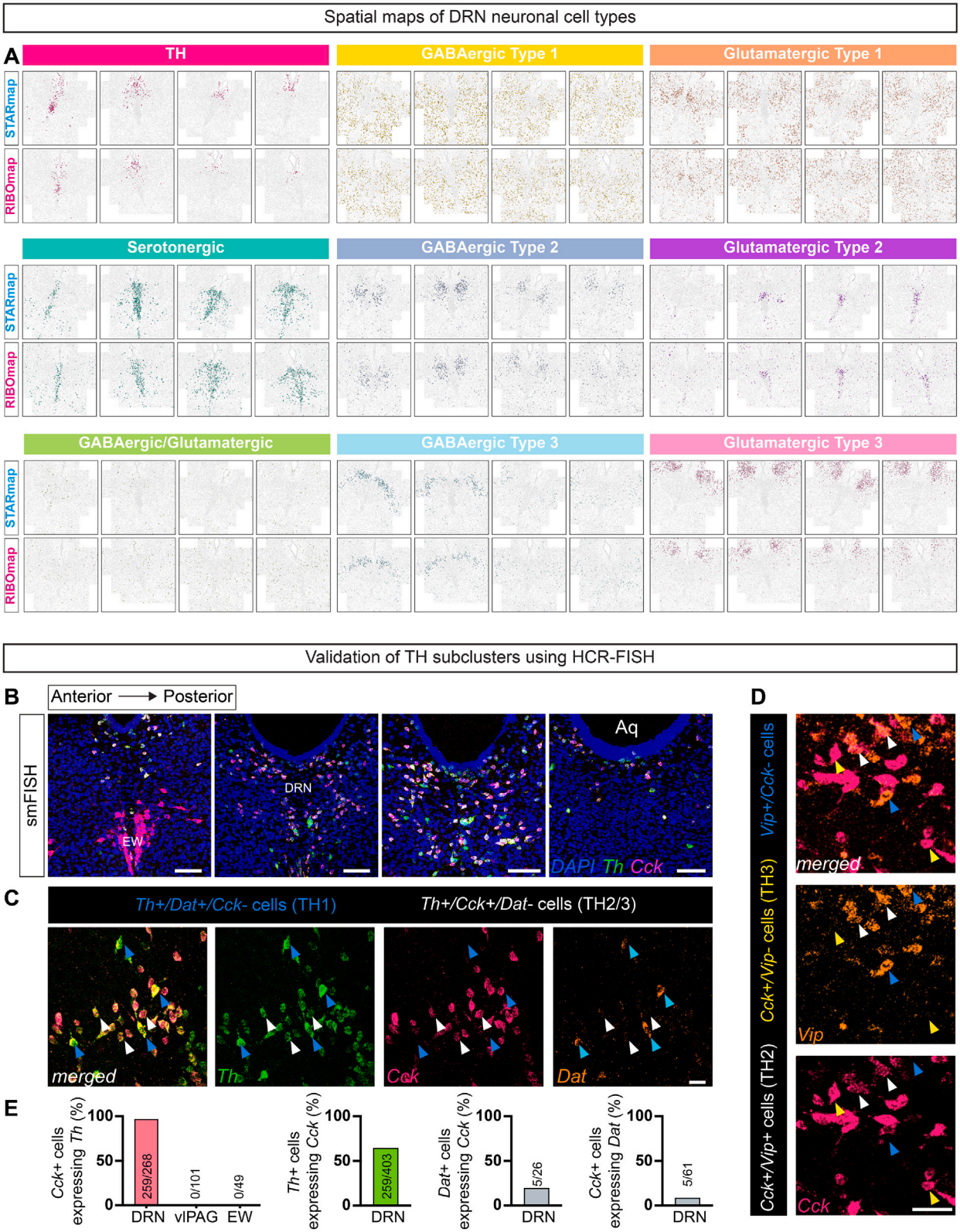

(legend on next page)

Figure S2. Spatial distributions of DRN neurons and validation of *Th*+ subclusters, related to Figure 1

(A) Spatial distribution of each neuronal cluster across the anterior-posterior axis for STARmap/RIBOmap studies.

(B) Representative smFISH images showing expression of *Th* (green) and *Cck* (pink) mRNA in the dorsal midbrain.

(C) Representative image of *Cck* (pink), *Th* (green), and *Dat* (orange) expression in the DRN. White arrowheads, *Th*+/*Cck*+/*Dat*− cells (TH2/3 subcluster). Cyan arrowheads, *Th*+/*Dat*+/*Cck*− cells (TH1 subcluster).

(D) Representative image of *Cck* (pink) and *Vip* (orange) expression in DRN. White arrowheads, *Cck*+/*Vip*+ cells (TH2 subcluster). Yellow arrowheads, *Cck*+/*Vip*− cells (TH3 subcluster). Cyan arrowheads, *Vip*+/*Cck*− cells.

(E) Quantification of marker gene overlap from smFISH images (n = 6 sections across two mice).

Scale bar, 100 μm (B), 25 μm (C and D).

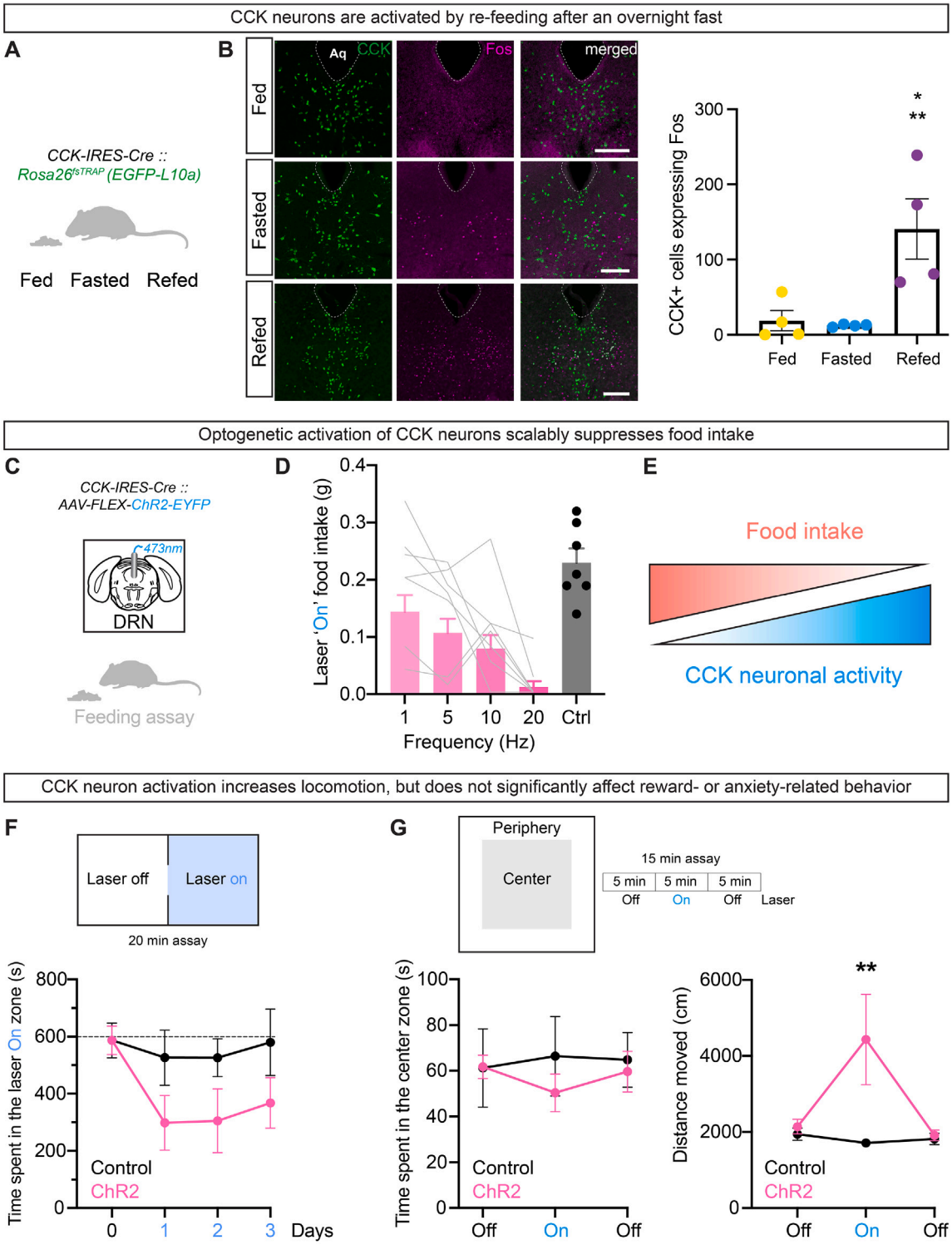

Figure S3. Activity profiling and manipulation of CCK neurons, related to Figure 2

(A) Schema for Fos studies.

(B) IHC for Fos protein and CCK neurons (GFP labeling from reporter cross; left) and quantification of their overlap (right) (*$p < 0.05$ for Fed vs. Refed; **$p < 0.01$ for Fasted vs. Refed; $n = 4$ mice per group).

(C) Schema for optogenetic activation.

(D) CCK neurons scalably suppress feeding ($n = 7$ mice per group).

(legend continued on next page)

(E) Summary schema.
(F) CCK neurons do not significantly alter real-time place preference (n = 5 mice per group).
(G) Stimulation of CCK neurons increases locomotion but does not affect anxiety (n = 7 mice per group).
Scale bar, 200 μm. $^{*}p < 0.05$, $^{**}p < 0.01$. Data are presented as mean ± SEM.

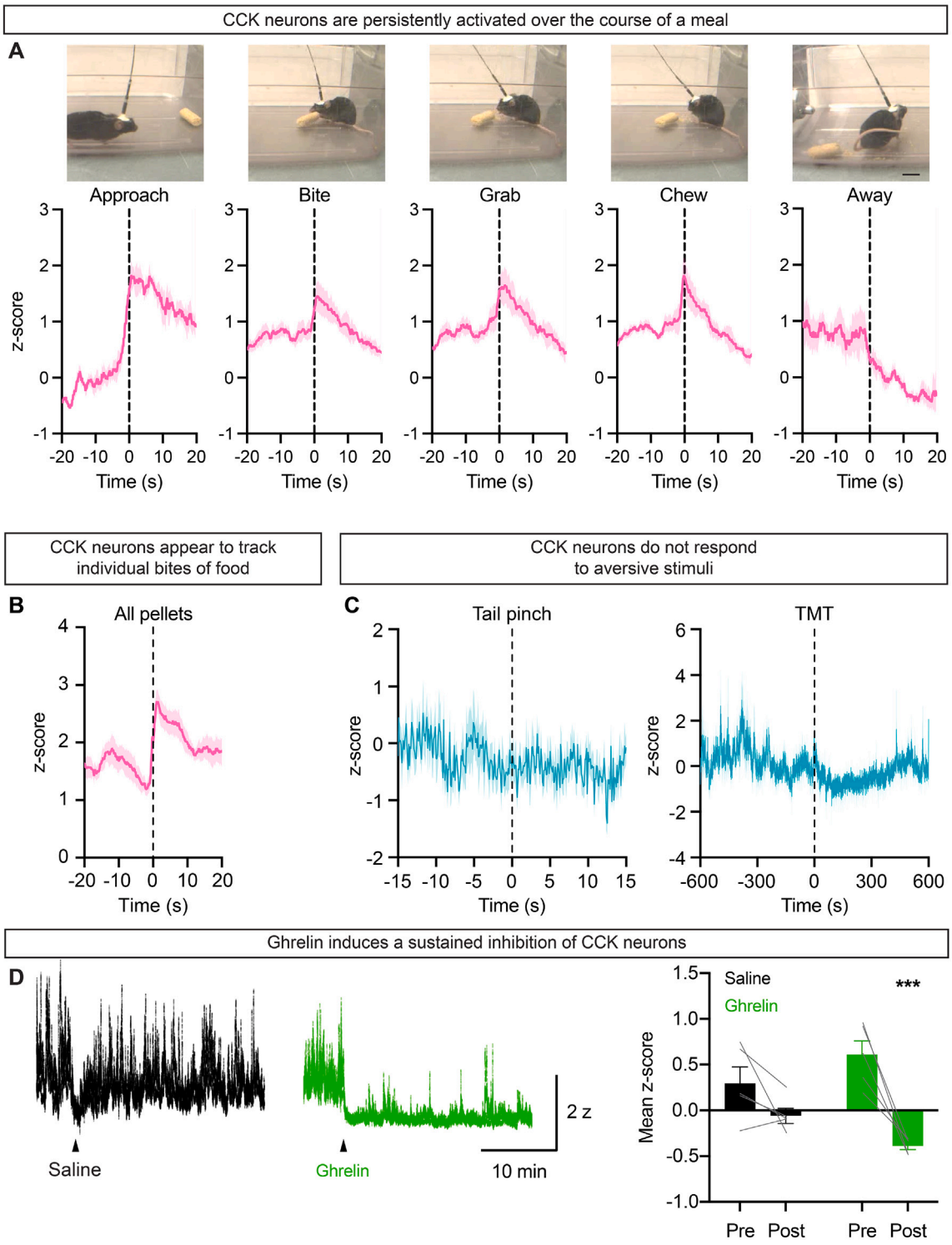

Figure S4. Fiber photometry recordings of CCK neurons, related to Figure 3

(A) Fiber photometry recordings of CCK neurons aligned to feeding behavior (images of video recordings are shown above traces; n = 4 mice).

(B) Averaged activity traces for all pellets consumed (n = 4 mice).

(C) Activity traces for CCK neurons with tail pinch (left) or fox odor (right) (n = 4–8 mice).

(D) Sample photometry traces (left) and aggregate analysis (right) comparing the effects of saline and ghrelin i.p. injections (n = 5 mice).

Scale bar, 2 cm. ***$p < 0.001$. Data are presented as mean ± SEM.

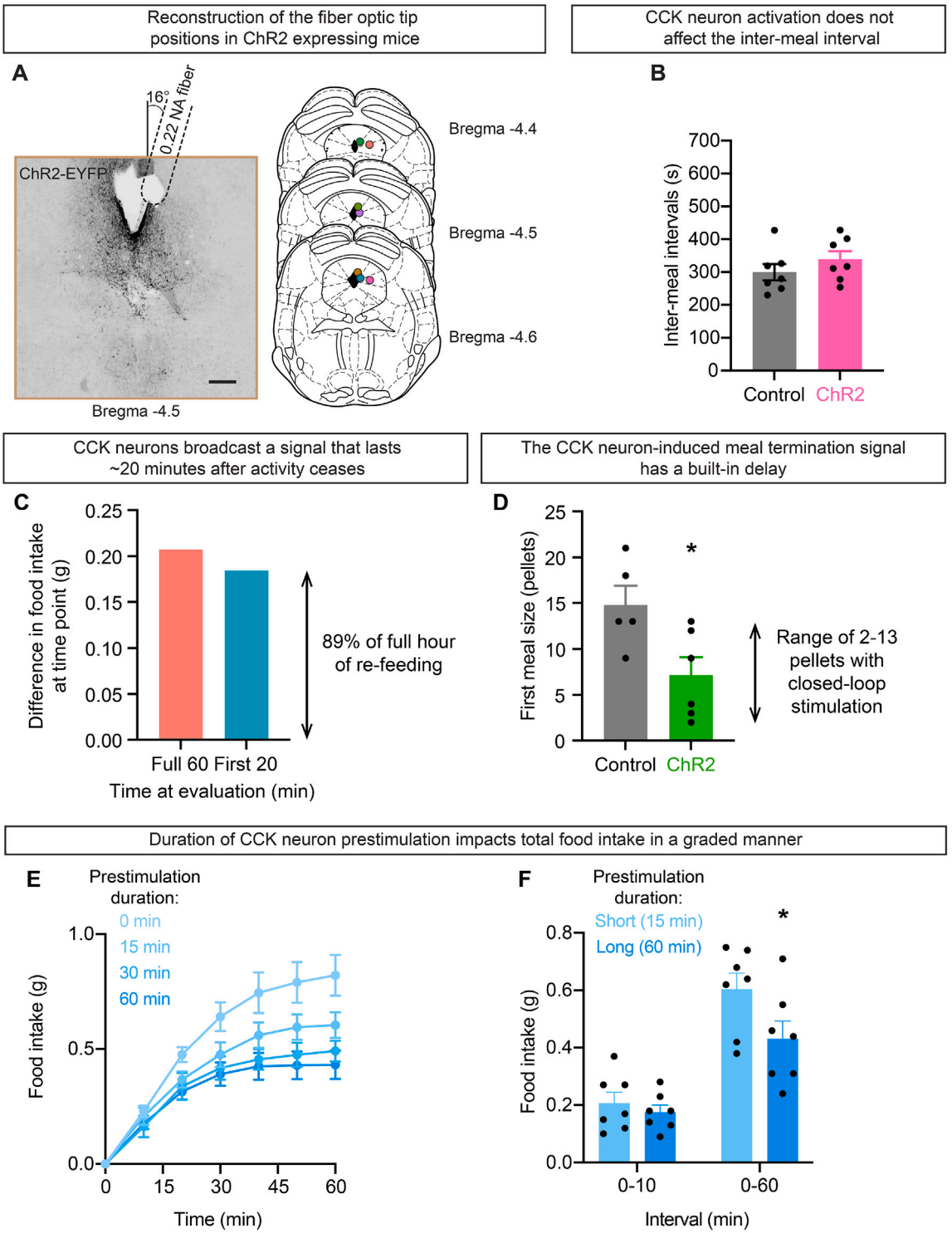

Figure S5. Feeding effects of optogenetic activation of CCK neurons, related to Figure 4

(A) Sample (left) and total (right) fiber placements for constant stimulation optogenetic studies.

(B) Inter-meal interval for optogenetic activation of CCK neurons (n = 7 mice per group).

(C) 89% of food intake suppression can be accounted for within the first 20 min of re-feeding after pre-stimulation.

(D) Closed-loop stimulation reduces meal size by about 50% (n = 5–6 mice per group).

(E and F) Pre-stimulation time of CCK neurons determines the magnitude of appetite suppression (E), acting on a delay (F) (n = 7 mice).

Scale bar, 200 μm. *$p < 0.05$. Data are presented as mean ± SEM.

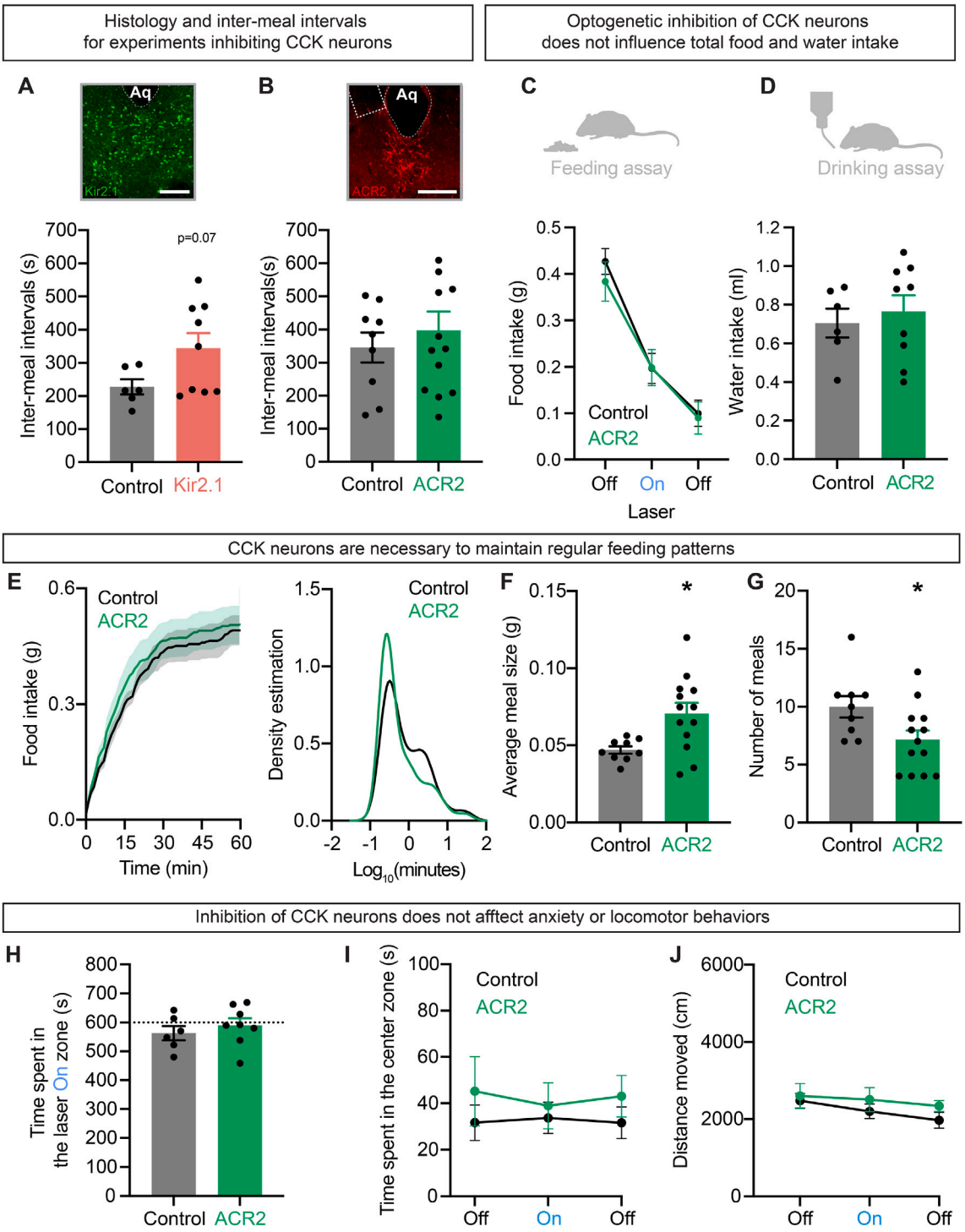

Figure S6. Loss-of-function studies for CCK neurons, related to Figure 4

(A) Sample viral expression (top) and inter-meal intervals (bottom) for Kir2.1 studies (n = 6–9 mice per group).

(B) Sample viral expression and fiber placement (top), as well as inter-meal intervals (bottom) for ACR2 studies (n = 6–9 mice per group).

(C and D) ACR2-mediated CCK neuron inhibition does not acutely alter total food (C) or water intake (D) (n = 6–9 mice per group).

(E) ACR2-mediated CCK neuron inhibition alters feeding microstructure (right), without altering total food intake (left).

(F and G) ACR2-mediated inhibition of CCK neurons increases average meal size (F) while suppressing total meal number (G) (n = 9–13 mice per group).

(H–J) ACR2-mediated CCK neuron inhibition has no effect on reward (H), anxiety (I), or locomotor (J) behaviors (n = 6–8 mice per group).

Scale bar, 200 μm. *p < 0.05. Data are presented as mean ± SEM.

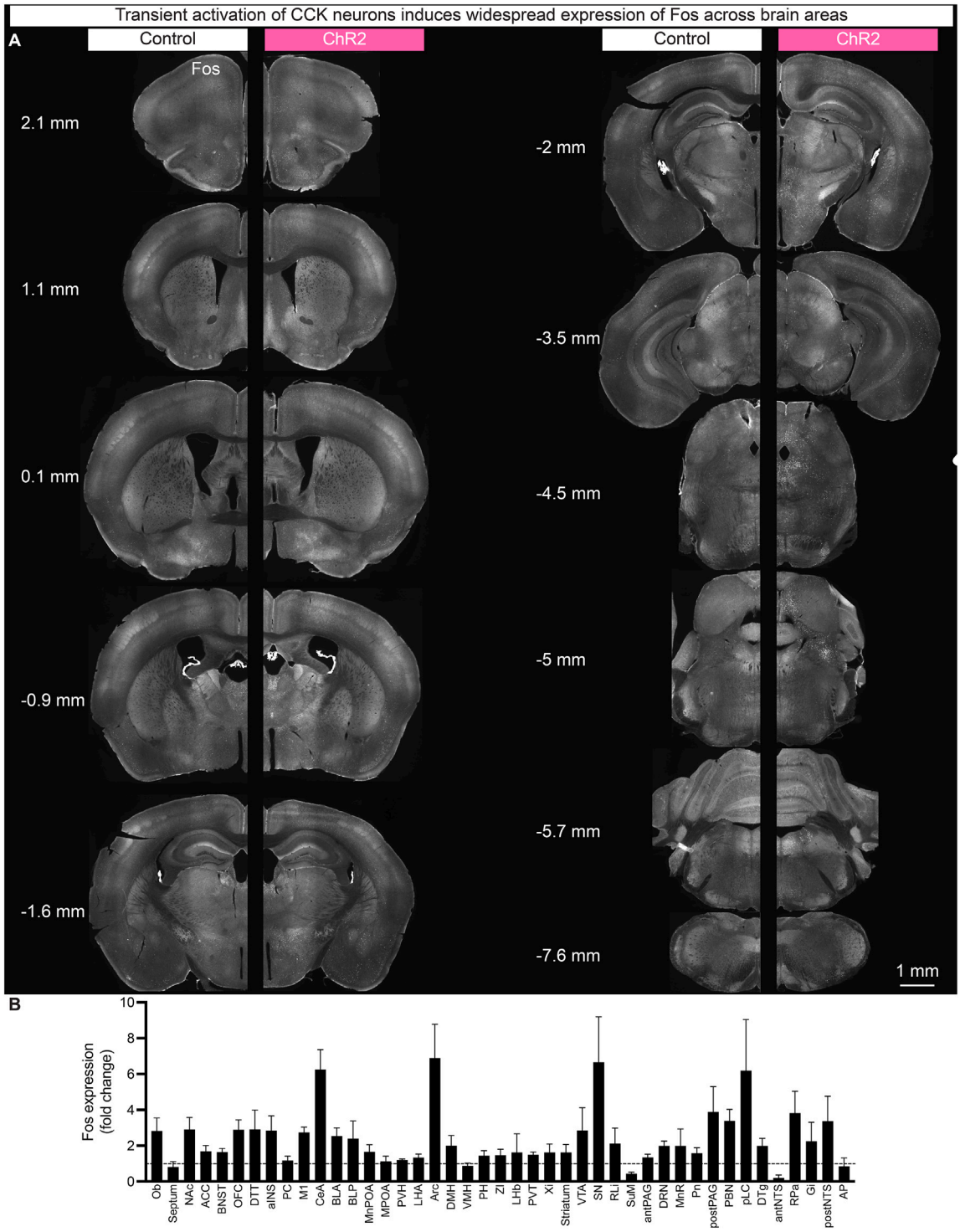

Figure S7. Whole-brain Fos mapping after CCK activation, related to Figure 6

(A and B) Representative images (A) and relative Fos expression (fold change over control) (B) across the brain (n = 3–4 mice per group). Numbers next to coronal sections indicate approximate coordinates relative to bregma. Regions in (B) are arranged anterior to posterior.

Scale bar, 1 mm. Data are presented as mean ± SEM.